Statistical properties in the quasi-continuum of atomic nuclei

Ann-Cecilie Larsen
Department of Physics
University of Oslo
May, 2008

Dissertation presented for the degree of
Philosophiae Doctor (PhD) in Physics

Series of dissertations submitted to the
Faculty of Mathematics and Natural Sciences, University of Oslo
Nr. 733

ISSN 1501-7710

Cover: Inger Sandved Anfinsen.
Printed in Norway: AiT e-dit AS, Oslo, 2008.

Produced in co-operation with Unipub AS.
The thesis is produced by Unipub AS merely in connection with the
thesis defence. Kindly direct all inquiries regarding the thesis to the copyright
holder or the unit which grants the doctorate.

Unipub AS is owned by
The University Foundation for Student Life (SiO)

Preface

In 1911, Rutherford discovered the existence of the atomic nucleus, which was later confirmed through the experiments of Geiger and Marsden. A new branch of science, nuclear physics, started to develop. In the 1940s and 1950s, it was revealed that protons and neutrons, which are the constituents of the nucleus, were not fundamental, but built up of even smaller particles later called quarks and gluons. However, some of the most fundamental problems of nuclear physics such as the exact nature of the force that holds the nucleus together, are yet unsolved. In recent years, a huge effort has been made to understand the basic force between the quarks and gluons, and attempts have been made to describe nuclear properties from first principles. However, the complex nature of the nuclear force makes this task extremely hard. The status of today is that nuclear physics still lacks a coherent theoretical formulation that would enable us to analyze and interpret all nuclear phenomena in a fundamental way.

The aim of this thesis is to provide a tiny bit of new insight into the broad and diverse field of nuclear physics by presenting experimental observations on statistical properties of medium-mass nuclei at high temperatures. This has long been the main research field of the nuclear physics group at the Oslo Cyclotron Laboratory, where the experiments were performed. In the experiments, the nuclei were excited to high-energy quantum levels and the decay from these levels were studied by means of statistical methods. This thesis will show that statistical methods are applicable in the energy region of interest, even for relatively small systems such as a nucleus, provided that the nucleus is brought to a sufficiently high temperature and that the time scale is large enough for the nucleus to equilibrate before emitting radiation. The results are especially interesting from an astrophysical point of view, as the nuclear structure close to the particle separation energies influences strongly the nucleosynthesis processes that take place in extreme stellar environments such as supernovae.

Acknowledgments

First, my superb supervisors John B. Rekstad and Sunniva Siem deserve a heap of thanks for always being inspiring, supportive and helpful. Many thanks for all the nuclear physics discussions, and your proofreading of this thesis. I am indebted to John for helping me out with methodical details and lots of questions, and to Sunniva who did a great job with all the administrative issues in addition to the scientific and social part. You are clever and talented nuclear scientists, and I have learnt so much from you.

I am deeply grateful to the whole nuclear physics group at the Oslo Cyclotron Laboratory. You make the working day easy and pleasant. It is always fun to go together to conferences and experiments abroad. Special thanks to my room mate Naeem U. H. Syed for all nice discussions and conversations. Many thanks to Rositsa Chankova, Finn Ingebretsen, Svein Messelt, and Stein Ødegård for taking shifts during the experiments and your helpful comments. Finn, thanks for lending me the Peanuts cartoons. Many thanks to Alexander Bürger for the careful reading of this thesis, that was of great help. Also, I would like to thank Hilde T. Nyhus and Heidi K. Toft that helped me baking birthday cakes and freed me from boring committee meetings in the stressful and critical time when the thesis was finished.

I am very thankful to the excellent engineers of the Cyclotron Laboratory, Eivind A. Olsen and Jon C. Wikne for their outstanding work keeping the cyclotron and the lab computers in good shape, and for providing great experimental conditions during the campaigns. I have learned much from you, especially which knobs one should and should *not* touch at the cyclotron control panel.

I am indebted to Andreas Schiller and Alexander Voinov from Ohio University. You have both been of tremendous help and have been deeply involved in this project, and I have learnt so much from you. I am also grateful to Steve M. Grimes and all the collaborators at Ohio University. I would like to express my gratitude to Undraa Agvaanluvsan and Lee Bernstein at Lawrence Livermore National Laboratory, Emel Algin from Osmangazi University, and Gary E. Mitchell from North Carolina State University for your contributions, support and illuminating discussions. Special thanks to Tom Lönnroth from Åbo Akademi University for letting me be responsible for the vanadium data. You were always the winner of the night-shift competition during the experiments. I hope you will find some time to build more model trains.

Finally, I wish to give many thanks to my dear family. I am grateful to

my parents, Ann-Vilde and Hans-Peder, and my sister Beate, for their love and support through all these years. Magne, I cannot thank you enough for all your help in every aspects and stages of this work. You have the knowledge of every detail of the experimental setup and the analysis, and you have a deep insight in nuclear physics. From now on, since the thesis is finished and there should be no more working late at night, I promise to take our dog Romeo out in the morning.

Ann-Cecilie Larsen

May 7, 2008

Contents

List of Figures

List of Tables

Chapter 1

Introduction

Low-energy nuclear physics describes atomic nuclei in terms of nucleons as the relevant degrees of freedom. The carriers of the force between the nucleons are thought to be light mesons, in particular the π and ρ mesons. *Ab initio* calculations based on, e.g, the shell model, are able to describe the observed nuclear quantum numbers such as energy levels, spin and parity with good accuracy for nuclei and excitation energies where there are relatively few quantum energy levels accessible. Transition strengths and branching ratios are also often well reproduced.

However, as the excitation energy increases, the density of energy levels becomes so high that it is impractical or even impossible to resolve individual levels. This is the region of the quasi-continuum, squeezed in between the discrete region where levels are easily resolved with state-of-the-art spectroscopy measurements, and the continuum region, where the levels are overlapping and thus not possible to separate. The onset of quasi-continuum varies from nucleus to nucleus, and is in general at higher excitation energy for light nuclei and nuclei with nucleon numbers close to or equal a magic number – that is, a filled major shell[1].

In the region of quasi-continuum, the precise location of levels and strengths of individual transitions between those levels is of much lesser importance than in the discrete region. The mixing that occurs due to small, residual interactions dilutes the purity of, in principle, simple excitations formulated in terms of approximate quantum numbers. The strength of these excitations is then distributed over many energy levels. Therefore, statistical concepts such as average values and fluctuations around those values become the physically relevant quantities.

Two very important, statistical quantities applied in the quasi-continuum,

[1]The magic numbers representing shell closures are 2, 8, 20, 28, 50, 82, and 126 [1].

is the nuclear level density and the γ-ray strength function. These average quantities can be regarded as the counterparts of the energy levels and transition strengths in the discrete region. Local deviations from a smooth behaviour in the level density and the strength function imply global structure changes in the nucleus, such as breaking of nucleon Cooper pairs or collective excitation modes such as the scissors mode.

However, it has has proven to be a difficult task to get experimental information on the level density and the γ-ray strength function in the medium and high excitation-energy region. The nuclear physics group at the Oslo Cyclotron Laboratory (OCL) has developed a method (the so-called Oslo method) to extract level density and γ-ray strength function from first-generation γ-ray spectra for excitation energies between the ground state and the neutron (proton) binding energy [2, 3, 4]. This unique technique has provided experimental evidence for the sequential breaking of nucleon Cooper pairs [5] and an M1 scissors mode pygmy resonance in rare-earth nuclei [6, 7]. Also, a strongly enhanced strength function at low γ energies has been discovered in several Fe and Mo isotopes [8, 9].

The main object of this thesis is to investigate how the level density and the γ-ray strength function develop in medium-mass nuclei, and to test the Oslo method on nuclei with neutron or proton numbers near or at magic numbers. Therefore, the nuclei studied here are $^{44,45}_{21}$Sc [10, 11], $^{50,51}_{23}$V [12], and $^{93-98}_{42}$Mo [9, 13]. The Sc nuclei are close to the proton shell $Z = 20$, while the neutrons are filling the $f_{7/2}$ shell half-way. The situation is opposite in ^{50,51}V, with 23 protons and with a closed or almost closed $N = 28$ shell for ^{51}V and ^{50}V, respectively. Moving to a region of heavier nuclei, the Mo isotopes considered in this thesis have neutron numbers near the $N = 50$ shell closure. Shell effects are therefore expected to manifest themselves in the level density through structures and an overall lower level density than for mid-shell nuclei. Such features will be looked for in the presented experimental data.

When it comes to the γ-ray strength functions, it is an open question whether the low-energy enhancement seen in the Fe and Mo isotopes is a feature related to specific structures in these nuclei, or if it is a general behaviour of nuclei in a certain mass region. This issue has been addressed in the present work.

The thesis is organized as follows: Chapter 2 gives a historic overview of theoretical and experimental achievements concerning level densities and γ-ray strength functions. In Chapter 3, the experimental equipment and some details of the performed experiments are given, and the data analysis is briefly described. The Oslo method is explained and discussed

in Chapter 4. Chapter 5 includes reprints of five published articles. Finally, conclusions and an outlook will be given in Chapter 6.

Chapter 2

Nuclear structure and γ-ray strength in the quasi-continuum

The excitation-energy region between the discrete regime (where the nuclear states have well-defined quantum numbers), and the continuum region (where individual levels cannot be resolved due to minuscule or vanishing level spacings), is defined as the quasi-continuum. Here, the nucleus undergoes a transition from an ordered phase at low excitation energy to a more chaotic behaviour as the energy is increased. Nuclei in this transitional excitation-energy region might be most appropriately described by average quantities like the level density and the γ-ray strength function. The level density, averaged over a specific excitation-energy bin, replaces the counting of discrete levels, while the γ-ray strength function inherits the role that transition probabilities are playing at low excitation energies.

2.1 The level density

The level density is defined as the number of quantum energy levels accessible at a specific excitation energy, within a given energy bin. The level density gives direct information on thermodynamic properties of the nuclear system, see Appendix A for a brief introduction to thermodynamic concepts and quantities.

The first theoretical attempt to describe nuclear level densities was done by H. Bethe in 1936 [15]. In his fundamental and pioneering work, Bethe described the nucleus as a gas of non-interacting fermions moving freely in equally spaced single-particle orbits. The level density was obtained by the inverse Laplace transformation of the partition function

determined from Fermi statistics. Bethe's original results yielded a level density function

$$\rho(E) = \frac{\sqrt{\pi}}{12}\frac{\exp(2\sqrt{aE})}{a^{1/4}E^{5/4}}, \tag{2.1}$$

for an excitation energy E, and where a is the level-density parameter given by

$$a = \frac{\pi}{6}(g_{\mathrm{p}} + g_{\mathrm{n}}). \tag{2.2}$$

The terms g_{p} and g_{n} are the single-particle level density parameters for protons and neutrons, respectively, which are expected to be proportional to the mass number A. In fact, Bethe's consideration of the nucleus to be a Fermi gas of free protons and neutrons confined to the nuclear volume gives

$$a = \alpha A. \tag{2.3}$$

The constant α has been found to be about $1/8 - 1/10$ by fitting to experimental data.

The Bethe expression predicts an exponential increase in the level density with the square-root of the excitation energy and level-density parameter. This has been found to be qualitatively true, although important factors such as pairing correlations, collective phenomena and shell effects are not included. Refined versions of the original Fermi gas formula take into account these effects by employing free parameters that are adjusted to fit experimental data on level spacings obtained from neutron and/or proton resonance experiments. A. Gilbert and A. G. W. Cameron [16] proposed the following level-density formula in 1965:

$$\rho(U) = \frac{\sqrt{\pi}}{12}\frac{\exp(2\sqrt{aU})}{a^{1/4}U^{5/4}}\frac{1}{\sqrt{2\pi}\sigma}. \tag{2.4}$$

Here, U is the shifted excitation energy, $U = E - \Delta_{\mathrm{p}} - \Delta_{\mathrm{n}}$, where Δ_{p} and Δ_{n} are the pairing energy for protons and neutrons, respectively. The spin cutoff parameter σ is given by

$$\sigma^2 = g\langle m^2\rangle T, \tag{2.5}$$

where $g = g_{\mathrm{p}} + g_{\mathrm{n}}$ relate to the level density parameter as in Eq. (2.2), $\langle m^2\rangle \approx 0.146A^{2/3}$ is the mean-square magnetic quantum number for single-particle states, and the temperature is given by

$$T = \sqrt{U/a}. \tag{2.6}$$

Another expression of the level density for excitation energies between $0 - 10$ MeV is obtained from the constant-temperature (CT) model [16],

$$\rho(E) = \frac{1}{T}\exp[(E - E_0)/T], \tag{2.7}$$

where E is the excitation energy, and the free parameters T and E_0 are connected to a constant nuclear temperature (in contrast to Eq. (2.6)) and an energy shift, respectively.

A variant of the shifted Gilbert-Cameron expression given in Eq. (2.4) is the back-shifted Fermi gas (BSFG) model [17], where the level-density parameter and energy shift are considered as free parameters, allowing for a reasonable fit to experimental data over a wider range of energies[1]. Also, phenomenological methods were developed to describe the energy dependence of the parameter a.

In 2005, T. von Egidy and D. Bucurescu [18] published a new compilation of systematics of nuclear level-density parameters. In their approach, they determined a new set of phenomenological level density parameters for the BSFG and CT model by fitting the latest data on low-excitation-energy levels and neutron resonance spacings at the neutron binding energies for 310 nuclei between ^{19}F and ^{251}Cf. Then they studied the variations of these parameters for the set of nuclei, and observed correlations with other physical observables leading to the determination of simple formulas that describe the main features of the empirical parameters. For the BSFG model, the following expressions were used for the level density and the spin cutoff parameter:

$$\rho(E) = \frac{\exp[2\sqrt{a(E - E_1)}]}{12\sqrt{2}\sigma a^{1/4}(E - E_1)^{5/4}} \tag{2.8}$$

and

$$\sigma^2 = 0.0146A^{5/3}\frac{1 + \sqrt{1 + 4a(E - E_1)}}{2a}. \tag{2.9}$$

The level-density parameter a and energy shift E_1 were treated as free parameters to be fitted to experimental data.

The expression for σ is based on the rigid-body value for the nuclear moment of inertia,

$$\mathcal{I} = \frac{2}{5}\frac{m_0 r_0^2}{\hbar^2}A^{5/3}, \tag{2.10}$$

[1]The shift $\Delta_p + \Delta_n$ turns out to be too large, so it is 'back-shifted' by subtracting a parameter C_1 [17].

where m_0 is the nucleon mass and r_0 is the nuclear radius parameter, and the nuclear temperature is described as

$$T = \frac{1 + \sqrt{1 + 4a(E - E_1)}}{2a}. \tag{2.11}$$

From the relation

$$\sigma^2 = \mathcal{I}T, \tag{2.12}$$

we obtain the expresion given in Eq. (2.9). Although Eq. (2.11) has been shown to be mathematically incorrect in [16], the authors of [18] found Eq. (2.9) to be most adequate in the excitation-energy region considered in their work.

Other semi-empirical level density models have also been developed, such as the model by Kataria, Ramamurthy and Kapoor (KRK), which accounts for shell effects in terms of the ground-state shell correction to the nuclear binding energy, and the Generalized Superfluid (GSF) model introduced by Ignatyuk and others. As these models will not be used in this thesis, the reader is referred to [19] and references therein for further information.

Although the above-mentioned semi-empirical expressions give reasonable agreement with experimental data on, e.g., neutron resonance spacings, they are not able to describe fine structures in the level density caused by pair breaking, shell effects etc. Also, any extrapolation to nuclei far from the valley of stability where little or no experimental data are known could be highly uncertain. In order to have a predictive power, level densities should ideally be calculated from microscopic models based on first principles and fundamental interactions.

For a detailed, microscopic description of the nuclear level density, one should solve the exact many-body eigenvalue problem

$$\hat{H} \left| \Psi \right\rangle = E \left| \Psi \right\rangle, \tag{2.13}$$

where the Hamiltonian is given by

$$\hat{H} = \sum_{i=1}^{A} -\frac{\hbar^2}{2m} \nabla_i + \sum_{i<j}^{A} v(i,j) \tag{2.14}$$

assuming a two-body character of the nucleon interaction, and where i represents all relevant coordinates and quantum numbers of the ith nucleon. The nuclear wave function for A nucleons is given as

$$\left| \Psi \right\rangle = \left| \Psi(1, ..., A) \right\rangle. \tag{2.15}$$

This is a simplified, non-relativistic treatment where three-body and higher-order contributions are neglected. However, this has turned out to be a tremendous challenge for mid-mass and heavy nuclei as the dimension of the problem grows rapidly with the number of nucleons. For example, using the interactive shell model to simplify the Hamiltonian and provide an orthogonal basis for single-particle wave functions, the required model space is many orders of magnitude larger than spaces in which conventional diagonalization methods can be applied. It is therefore of great importance to introduce methods where level density can be calculated approximately without loosing too much of the desired microscopic details.

One such method is the shell model Monte Carlo approach as applied by Y. Alhassid *et al*. [20, 21, 22]. Here, thermal averages are taken over all possible states of a given nucleus. Two-body correlations are fully taken into account within the model space[2]. These calculations show very promising results and are often in good agreement with experimental data. The drawback is that they are very time consuming.

Another statistical approach, starting from mean-field theory, is presented by P. Demetriou and S. Goriely [23]. Here, a global, microscopic prescription of the level density is derived based on the Hartree-Fock-BCS (HFBCS) ground-state properties (single-particle level scheme and pairing force). Combinatorial models have also been developed [24], which, like the HFBCS plus statistical model, give almost equally good agreement with experimental data as obtained with phenomenological BSFG formulae. A global combinatorial model has been combined with an updated deformed Hartree-Fock-Bogolyubov model by S. Hilaire and S. Goriely [25], where the combinatorial predictions provide the non-statistical limit that by definition cannot be described by any statistical approach. Another advantage of this combined model is that the parity dependence of the level density is obtained in addition to the energy and spin dependence. Globally, the new model of [25] predicts s- and p-wave neutron resonance spacing data within a factor of two.

When it comes to measuring level densities experimentally, several methods have been developed and applied in various excitation-energy regions. At low excitation energies it is possible to determine the level density by counting the discrete levels from databases such as the Table of Isotopes [26] and ENSDF [27]. However, this method quickly becomes unreliable when the level density reaches about 50 levels per MeV.

[2]The complete *pf* shell and the $0g_{9/2}$ orbit are included in calculations of nuclei from iron to germanium [21]).

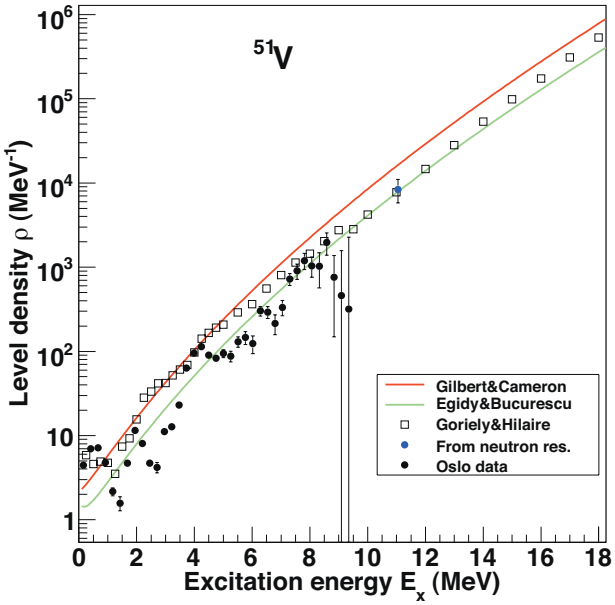

Figure 2.1: The level density of ^{51}V calculated with two parameterizations of the back-shifted Fermi gas model (colored lines, [17, 18]), and from the work of S. Hilaire and S. Goriely (white squares, [25]) compared to the experimental level density from OCL (black dots, [12]).

At the neutron (proton) separation energy, the numbers of s- and p-wave neutron (proton) resonances within the energy range of the incoming neutron (proton) reveal the level spacing between the states reached in the capture reaction [19]. This is the method of choice for determining parity- and spin-projected level density at and slightly above the neutron (proton) separation energy. Obviously, the method is not applicable at other energies, and corrections are needed for missing resonances or contaminating resonances with higher ℓ values.

Another appreciable method is the Hauser-Feshbach modelling of evaporation spectra [28]. This method can be applied to the quasi-continuum and produces reliable level density functions, including fine structures. However, care has to be taken so that the underlying assumptions of the Hauser-Feshbach theory are met by choosing appropriate reactions, beam

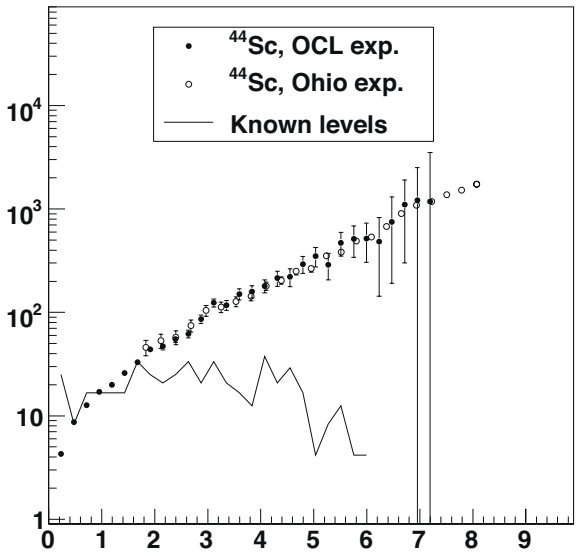

Figure 2.2: The level density of ^{44}Sc obtained from Hauser-Feshbach modelling of α-evaporation spectra (open circles) and from a statistical analysis of primary-γ spectra (black circles), see [11].

energies, ejectile angles and so on. Also, *a priori* knowledge of particle transmission coefficients is needed.

In the Ericsson regime (excitation energies $3-4$ MeV above the neutron separation energy for heavy nuclei), the level density can be determined from a fluctuation analysis of total neutron cross sections [29]. This method relies on specific assumptions concerning how level density can be extracted from cross-section fluctuations. In particular, level widths, level spacings and the experimental resolution must follow a certain hierarchy, which is only fulfilled in certain energy regions. Also the restriction to very specific reactions limits the usefulness of this method.

A recent method to measure the level density has been developed by the Oslo nuclear physics group [2, 3, 4]. This method, called the Oslo method, is based on a statistical analysis of primary-γ spectra extracted from various excitation-energy bins. The extracted level density of ^{51}V

is shown in Fig. 2.1, where it is compared with calculated level densities from the back-shifted Fermi gas model, and the calculations of [25]. The Oslo method determines the functional form of the level density between the discrete region and the neutron (or proton) separation energy, and has about the same precision in providing information on fine structures as the Hauser-Feshbach modelling of evaporation spectra, see Fig. 2.2. It is however necessary to use information on discrete levels and neutron (proton) resonances in order to obtain the correct slope and absolute value of the level density.

2.2 The γ-ray strength function

Gamma-ray strength functions characterize the average electromagnetic properties of excited nuclei, which means that they are closely connected to radiative decay and photo-absorption processes. They are also called radiative strength functions [30] and photon strength functions [31] in the literature. They can be directly associated with reduced transition probabilities, see Appendix B for details on this subject.

The original definition of a model-independent γ-ray strength function is (Bartholomew *et al*. [32]):

$$f_{XL}(E_\gamma) = \frac{\langle \Gamma_{\gamma\ell} \rangle}{(E_\gamma^{2L+1} D_\ell)} \,. \tag{2.16}$$

Here, $f_{XL}(E_\gamma)$ is the γ-ray strength for electromagnetic character X, multipolarity L, and γ-ray energy E_γ, $\langle \Gamma_{\gamma\ell} \rangle$ is the average radiative width and D_ℓ is the resonance spacing for ℓ-wave resonances (usually s- or p-wave) determined from average resonance capture (ARC) neutron experiments. This is the "downward" strength function related to the γ decay. The photo-excitation ("upward") strength function is determined by the average photo-absorption cross section $\langle \sigma_{XL}(E_\gamma) \rangle$ summed over all possible spins of final states [19, 31, 33]:

$$f_{XL}(E_\gamma) = \frac{1}{(2L+1)(\pi\hbar c)^2} \frac{\langle \sigma_{XL}(E_\gamma) \rangle}{E_\gamma^{(2L-1)}} \,. \tag{2.17}$$

Based on Fermi's golden rule and the principle of detailed balance, the "upward" and "downward" γ-ray strength function correspond to each other provided that the same states are populated.

The γ-ray strength function f_{XL} is related to the γ-ray transmission coefficient $\mathcal{T}_{XL}$ by

$$\mathcal{T}_{XL}(E_\gamma) = 2\pi E_\gamma^{(2L+1)} f_{XL}(E_\gamma)\,. \tag{2.18}$$

Therefore, γ-ray strength functions are important for the description of the γ emission channel in nuclear reactions. This is an almost universal channel since γ rays, in general, may accompany emission of any other emitted particle. Like the particle transmission coefficients that emerge from the optical model, γ-ray transmission coefficients enter the Hauser-Feshbach model for calculation of the competition between photon emission with other particles.

The simplest model for the strength function, the single-particle model of Blatt and Weisskopf [34], results in energy-independent strength functions. This has been long known to be a too simple picture – collective excitations must also be taken into account. For instance, the well-known giant electric dipole resonance (GEDR) that strongly influences the strength function has been observed throughout the periodic table with great regularity. This resonance is believed to stem from harmonic vibrations where protons and neutrons oscillate off-phase against each other, and is therefore called an *isovector* collective excitation mode. Other giant resonances have been discovered as well, such as the giant magnetic dipole resonance (GMDR), which is built of spin-flip transitions between $\ell \pm 1/2$ subshells, and the *isoscalar* giant electric quadrupole resonance (GEQR) originated from surface oscillations where the protons and neutrons are distorted in two orthogonal directions. For more information on giant resonances in general, see M. N. Harakeh and A. van der Woude [35].

There is also experimental evidence for other types of collective excitation modes, namely the so-called pygmy resonances, which are small compared to the corresponding giant resonances. Examples of such small resonances are the M1 scissors mode, where, in a macroscopic view, the proton and neutron clouds act like a pair of scissor blades "clipping" against each other, and the E1 pygmy resonance caused by a "skin" created by excess neutrons oscillating against an $N = Z$ core.

In the following, some of the standard models for the E1 strength function will be described. For details regarding the determination of various constants etc., and also for a description of the models of the M1 spin-flip and E2 isoscalar resonance, see Appendix C.

The Brink-Axel hypothesis [30, 36] has been widely used to describe collective excitation modes, and in particular the GEDR. The hypothesis states that collective excitations built on excited states have the same properties as those built on the ground state; that is, the probability of γ decay

is only dependent on the γ-ray energy and not on the temperature of the final state. This strong assumption leads to a Lorentzian shape of the giant resonances. For the GEDR, the Standard Lorentzian (SLO) is given as[3] [19]

$$f_{\mathrm{E1}}(E_\gamma) = \frac{1}{3\pi^2\hbar^2c^2}\frac{\sigma_r\Gamma_r^2E_\gamma}{(E_\gamma^2 - E_r^2)^2 + \Gamma_r^2E_\gamma^2} \tag{2.19}$$

in units of MeV^{-3}. Here, the Lorentzian parameters σ_r (in mb), Γ_r (in MeV) and E_r (in MeV) are the peak cross section, width and centroid energy of the GEDR, respectively. This form gives a very accurate description of photo-absorption data of mid-mass and heavy nuclei close to the resonance maximum. However, the SLO model significantly underestimates the γ-ray strength function for $E_\gamma \lesssim 1$ MeV. Also, the SLO model tends to overestimate experimental data such as capture cross sections and average radiative widths in heavy nuclei (see [19] and references therein).

In the work of Kadmenskiĭ, Markushev and Furman (KMF) based on Fermi liquid theory [37], a temperature dependency on the final states T_f is incorporated in the description of the GEDR:

$$f_{\mathrm{E1}}^{\mathrm{KMF}}(E_\gamma, T_f) = \frac{1}{3\pi^2\hbar^2c^2}\frac{0.7\sigma_r\Gamma_r^2(E_\gamma^2 + 4\pi^2T_f^2)}{E_r(E_\gamma^2 - E_r^2)^2} \tag{2.20}$$

Here, the temperature-dependent width of the GEDR is given by

$$\Gamma_{KMF}(E_\gamma, T_f) = \frac{\Gamma_r}{E_r^2}(E_\gamma^2 + 4\pi^2T_f^2), \tag{2.21}$$

where the first term reflects the spreading of particle-hole states into more complex configurations, and the second term accounts for collisions between quasiparticles. This temperature inclusion made it possible for the authors of [37] to reproduce quite accurately the experimental strength function of ^{144}Nd [38] in the region $E_\gamma = 0.2 - 7$ MeV. Also, the KMF model gives good agreement with capture cross sections and average radiative widths. However, using a variable temperature of the final states contradicts the Brink-Axel hypothesis. This could in principle be mended if a constant temperature is applied instead. Another problem with the KMF model is the divergence at the resonance centroid energy that makes it impossible to describe both the high- and low-energy part of the E1 strength function.

[3] The constant $1/(3\pi^2\hbar^2c^2) = 8.674 \cdot 10^{-8}$ $\mathrm{mb}^{-1}\mathrm{MeV}^{-2}$.

Several attempts have been made to implement the behavior of the strength function at low and high γ energies simultaneously. The Generalized Lorentzian (GLO) model as proposed by J. Kopecky and R. E. Chrien [39] consists of two terms: a Lorentzian with a temperature-dependent width according to Eq.(2.21), and the non-zero limit when $E_\gamma \rightarrow 0$ as described in [37]:

$$f_{\mathrm{E1}}^{\mathrm{GLO}}(E_\gamma, T_f) = \frac{1}{3\pi^2\hbar^2c^2}\sigma_r\Gamma_r \left[E_\gamma \frac{\Gamma_{KMF}(E_\gamma, T_f)}{(E_\gamma^2 - E_r^2)^2 + E_\gamma^2\Gamma_{KMF}^2(E_\gamma, T_f)} + 0.7\frac{\Gamma_{KMF}(E_\gamma = 0, T_f)}{E_r^3} \right]. \quad (2.22)$$

The GLO model gives reasonable agreement with data on capture cross sections and primary γ-ray spectra from ARC measurements for nearly spherical nuclei. For nuclei with a large ground-state deformation in the mass region $A = 150 - 170$, the GLO model underestimates the observed strength calculated from primary γ rays. Therefore, an Enhanced Generalized Lorentzian (EGLO) model has been proposed [19, 40], where a generalization of the temperature-dependent width is introduced as follows:

$$\Gamma_{\mathcal{K}}(E_\gamma, T_f) = \mathcal{K}(E_\gamma)\frac{\Gamma_r}{E_r^2}(E_\gamma^2 + 4\pi^2T_f^2), \quad (2.23)$$

where the empirical function $\mathcal{K}(E_\gamma)$ given by

$$\mathcal{K}(E_\gamma) = \kappa + (1 - \kappa)\frac{E_\gamma - E_0}{E_r - E_0} \quad (2.24)$$

relates the width in Eq. (2.21) to the collisional damping width in the Fermi liquid theory. The factor κ depends on the model adopted for the level density, while E_0 is a constant set to 4.5 MeV (see [19] and Appendix C).

From a theoretical point of view, there are problems with both the SLO and the (E)GLO models despite the good agreement of the latter with experimental results. As described in [19] and references therein, the shapes of the (E)GLO and SLO models are inconsistent with the general relationship between the γ-ray strength function of heated nuclei and the imaginary part of the nuclear response function to the electromagnetic field. Also, the damping width of the EGLO model is proportional to the collisional component of the damping width in the infinite Fermi liquid in which only the collisional (two-body) relaxation is considered. It is however necessary to also include the contribution from the fragmentation (one-body) width stemming from the nucleon motion in a self-consistent

mean field. This fragmentation width is almost independent of the temperature, and is not included in the (E)GLO model, while the temperature-independent width in the SLO model only accounts for the fragmentation, but not for collisional damping.

These shortcomings can be avoided using refined closed-form models such as the Modified Lorentzian (MLO) [19, 41, 42] given by

$$f_{\mathrm{E1}}^{\mathrm{MLO}}(E_\gamma, T_f) = \frac{1}{3\pi^2\hbar^2c^2}\mathcal{L}(E_\gamma, T_f)\sigma_r\Gamma_r\frac{E_\gamma\Gamma(E_\gamma, T_f)}{(E_\gamma^2 - E_r^2)^2 + E_\gamma^2\Gamma^2(E_\gamma, T_f)}. \quad (2.25)$$

Equation (2.25) is consistent with the principle of detailed balance, and is obtained by calculating the average radiative width of nuclei with micro-canonically distributed initial states. The term

$$\mathcal{L}(E_\gamma, T_f) = \frac{1}{1 - \exp(-E_\gamma/T_f)} \quad (2.26)$$

is a scaling factor that determines the enhancement of the γ-ray strength function in a heated nucleus as compared to a cold nucleus. This quantity can be interpreted as the average number of one-particle $-$ one-hole states excited by an electromagnetic field with frequency $\omega = E_\gamma/\hbar$, and is only important for low-energy γ rays [19]. The semi-empirical damping width is expressed as

$$\Gamma(E_\gamma, T_f) = \Gamma_C(E_\gamma, T_f) + \Gamma_F(E_\gamma), \quad (2.27)$$

where Γ_C represents the collisional damping width and Γ_F simulates the fragmentation component of the total damping width (see Appendix C for more details).

Another approach for the E1 strength function is the Generalized Fermi Liquid (GFL) model as proposed by S. F. Mughabghab and C. L. Dunford [43] and slightly modified in [19]. The GFL model depends on the final temperature T_f and the deformation parameter β_2, and is given by

$$f_{\mathrm{E1}}^{\mathrm{GFL}}(E_\gamma, T_f, \beta_2) = \frac{1}{3\pi^2\hbar^2c^2}\sigma_r\Gamma_r\frac{\mathcal{K}_{\mathrm{GFL}}E_\gamma\Gamma_m(E_\gamma, T_f)}{(E_\gamma^2 - E_r^2)^2 + \mathcal{K}_{\mathrm{GFL}}E_\gamma^2\Gamma_m^2(E_\gamma, T_f)}, \quad (2.28)$$

$$\mathcal{K}_{\mathrm{GFL}} = \sqrt{\frac{1 + F_1'/3}{1 + F_0'}}, \quad (2.29)$$

where F_0' and F_1' are the Landau-Migdal parameters of the quasi-particle interaction in the isovector channel of the Fermi system. According to [19],

the term $\mathcal{K}_{\mathrm{GFL}} E_\gamma^2 \Gamma_m^2(E_\gamma, T_f)$ is added in the denominator to avoid singularity at the resonance centroid energy. Equation (2.28) is thus an extension of the original expression given in [43]. Quite similar to the width in Eq. (2.27), the width Γ_m is given by a sum of a collisional damping width Γ_C and the term Γ_{dq} that simulates the fragmentation width:

$$\Gamma_m(E_\gamma, T_f) = \Gamma_C(E_\gamma, T_f) + \Gamma_{\mathrm{dq}}(E_\gamma, \beta_2). \tag{2.30}$$

The Hybrid Formula proposed by S. Goriely in Ref. [44] is another model that is able to simultaneously describe the low-energy and high-energy part of the γ-ray strength function. The form of the Hybrid Formula as given in [19] is:

$$f_{\mathrm{E1}}^{\mathrm{HF}}(E_\gamma, T_f) = \frac{1}{3\pi^2\hbar^2c^2}\sigma_r\Gamma_r \frac{E_\gamma \Gamma_h(E_\gamma, T_f)}{(E_\gamma^2 - E_r^2)^2 + E_\gamma^2\Gamma_r\Gamma_h(E_\gamma, T_f)}, \tag{2.31}$$

where

$$\Gamma_h(E_\gamma, T_f) = \mathcal{K}_{\mathrm{GFL}}\Gamma_r \frac{E_\gamma^2 + 4\pi^2T_f^2}{E_\gamma E_r}. \tag{2.32}$$

All expressions discussed so far need to be generalized for deformed nuclei, where the deformation leads to a splitting of the GEDR into two components corresponding to two oscillation frequencies, one for each principal axis. The E1 strength function in deformed nuclei is thus defined as the sum of two components, each with the corresponding centroid energy $E_{r,j}$, damping width $\Gamma_{r,j}$ and peak value of the photo-absorption cross section $\sigma_{r,j}$ where $j = 1$ and $j = 2$ correspond to collective vibrations along and perpendicular to the symmetry axis (see Appendix C for further details). In Fig. 2.3, model calculations are shown for the E1 strength function of ^{51}V, and it is seen how the models might deviate significantly at the low- and high-energy tails of the GEDR. The models of the M1 and E2 resonance briefly described in Appendix C are also included in the figure.

As for the level density, a microscopic treatment of the strength function is necessary to obtain information on the underlying nuclear structure and to have predictive power throughout the nuclear chart. For example, structures due to the scissors mode and neutron skin oscillations are not dealt with in a comprehensive way in the models described so far. Also, any extrapolation of the GEDR, GMDR and GEQR systematics for the resonance centroid energy, maximum cross section and damping width to exotic nuclei far from the β-stability line is highly questionable. Calculations based on, e.g., the random-phase approximation (RPA) have proven to be superior to the semi-classical approaches in predictive power.

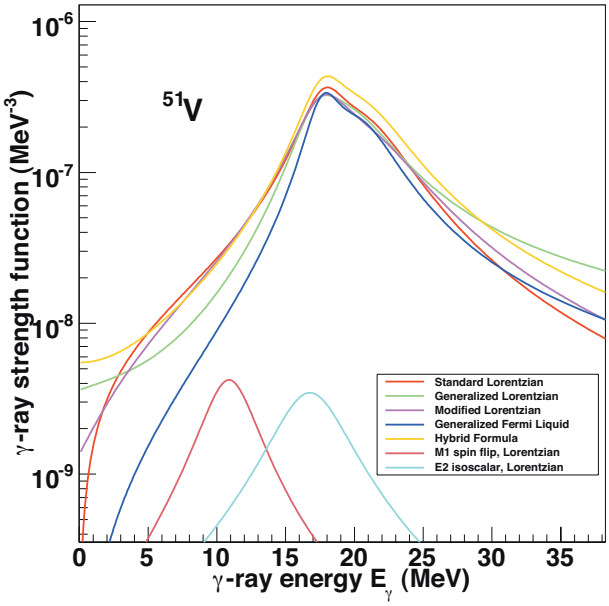

Figure 2.3: Various theories for the E1 strength in ^{51}V (see text) and the M1 spin-flip and E2 isoscalar resonance.

Several publications have been dedicated to the microscopic description of γ-ray strength functions. S. Goriely and E. Khan presented in Ref. [45] large-scale calculations based on the quasi-particle RPA (QRPA) model [46] to generate excited states on top of the HF+BCS ground state. To account for the damping of the collective motion, the GEDR is empirically broadened by folding the QRPA resonance strength with a Lorentzian function. These calculations were performed for more than 6000 nuclei with $8 \leq Z \leq 110$. It is shown that the QRPA provides a quite accurate description of the GEDR centroid and the fraction of the energy-weighted sum rule exhausted by the E1 mode (see [35] for a thorough treatment of radiative sum rules).

Another approach to treat the collective modes microscopically, is the quasi-particle multiphonon (QPM) model introduced by F. Andreozzi, F. Knapp, N. Lo Iudice, A. Porrino, and J. Kvasil [47]. Within this model, the nuclear eigenvalue problem given in Eq. (2.13) is solved exactly in a multi-

phonon space, where the basis states are generated via the Tamm-Dancoff Approximation (TDA) [46]. The calculations in Ref. [47] are compared with experimental data on low-lying negative parity states in ^{16}O, showing a fairly good agreement when three phonons ($3\hbar\omega$) are included. It appears that the isovector GEDR, which is harmonic, is not affected by the choice of number of phonons included. However, the strength distribution of the isoscalar GEQR is very sensitive to the size of the multiphonon space; if three phonons are included, much more fragmentation is induced compared to the case when only one phonon or two phonons are included. The same is true for octupole modes.

The by far largest contribution of experimental information on the γ-ray strength function is from photoabsorption measurements[4]. To measure photoabsorption, most often photoneutron cross sections, which provide a good substitute for photoabsorption cross sections, are measured. Photoneutron (or photoproton) cross-section measurements are dominated by E1 radiation, and are limited to energies above the neutron (proton) separation energy. Also, the absorption cross sections can only be measured on ground states or on very long-lived isomeric states. These measurements are traditionally performed by guiding a beam of photons to impinge on a thick target (typically several grams) of the nucleus that is under study. The photons can be of bremsstrahlung type from a betatron or a synchrotron facility, or produced by the in flight annihilation of fast positrons from a linear accelerator giving a quasi-monoenergetic photon beam although still containing some bremsstrahlung components [50, 51]. More recently, the inverse Compton-scattering technique has been utilized to produce true quasi-monoenergetic photon beams (see, e.g., Ref. [52] and references therein).

To measure the γ-ray strength function below the particle-emission threshold, photon scattering on isolated levels has been utilized. In the so-called Nuclear Resonance Fluorescence (NRF) method, the spins, parities, branching ratios and reduced transition probabilities of the excited states can be extracted in a model-independent way [53]. Polarization and angular correlation measurements allow the separation of transitions into E1, M1, and E2 transitions, usually with very good precision [54]. However, the method is selective with respect to strong transitions, and experimental thresholds might hamper the determination of an *average* transition strength as represented by the γ-ray strength function [6, 7, 55]. Never-

[4]See, e.g., the atlas of ground-state photoneutron and photoabsorption cross sections by S. S. Dietrich and B. L. Berman [48], and the Centre for Photonuclear Experiments Data [49].

theless, this method was able to confirm the experimental evidence for a new, low-lying magnetic dipole mode [53] first discovered in (e,e′) experiments [56] on rare-earth nuclei. Also, a thorough study of the E1 pygmy resonance in the ^{40,44,48}Ca isotopes and in $N = 82$ nuclei using photon scattering (γ,γ') reactions has been presented by A. Zilges *et al.* [57]. Here, a summed B(E1↑) strength of up to 1% of the Thomas-Reiche-Kuhn sum rule [35] for the total E1 strength was found for the pygmy resonance.

Another way of measuring γ-ray strength functions below the neutron separation energy, is by radiative neutron (or proton) capture reactions into compound states in the final nucleus [39, 58, 59]. From such experiments, both average total radiative widths of neutron resonances and individual transition strengths from one or several neutron resonances to one or several lower-lying discrete states can be obtained. Such primary γ-rays are averaged manually to get the γ-ray strength function, unless ARC neutrons were used, covering a wider range of energy and including many resonances. In the case of the total radiative widths, the γ-ray strength is obtained by integrating a modeled spectral distribution of γ rays which is constructed from trial γ-ray strength functions and level densities. In the analysis of individual transition strengths, corrections can be applied for, e.g., experimental bias and non-statistical effects. The advantage of measuring individual transition strengths is that since the spin and parity of both the initial and final states are known, E1, M1, and E2 γ-ray strength functions can be obtained separately. The method is however limited in energy in that it provides averages of transitions with energies in the order of $\sim 1-2$ MeV below the neutron separation energy.

Yet another approach in determining the γ-ray strength experimentally, is the spectrum-fitting method (see Ref. [60] and references therein). Within this method, a total γ-cascade spectrum is fitted in terms of trial γ-ray strength functions and level densities. This method has been used extensively for γ spectra following, e.g, fusion-evaporation reactions in the search for the temperature response of the giant electric dipole resonance and can cover a wide range of temperatures and spins. A special development of the spectrum-fitting method is the two-step cascade (TSC) or (n,2γ) method, where experimentally, only two-step cascades which connect neutron resonances and discrete low-lying levels with definite parity and spin are recorded. In this manner, the method trades flexibility in terms of applicable nuclear reactions, and temperature and spin regions with sensitivity to γ-ray strength functions of different multipolarities [6, 8, 55]. The disadvantage of all spectrum-fitting methods is that the level density remains a large source of systematic uncertainty, unless it is known *a priori*.

The Oslo method makes it possible to extract the γ-ray strength through the statistical analysis of excitation-energy indexed primary γ-ray spectra [4, 61]. This method is probably the most reliable method in terms of possible systematic errors to produce a total γ-ray strength function in the energy region below the neutron separation energy. It is therefore entirely complementary to the measurement of photoneutron and photoproton cross sections. The method is able to reveal fine structures, however, it does not provide absolute values and the γ-ray strength function has to be normalized to the average total radiative neutron resonance width. In several cases, the results from the Oslo method have been validated by their successful application to the spectrum-fitting method of total and two-step cascades [6, 8]. Also, the results after normalization to the average total radiative neutron resonance width are shown to be in excellent agreement with extrapolations of γ-ray strength from photoneutron cross-section measurements as well as individual transition strengths from neutron resonances [14].

Chapter 3

Experimental details and data analysis

3.1 Introduction

The experiments were performed at the Oslo Cyclotron Laboratory (OCL) at the University of Oslo. The cyclotron at the OCL is the heart and workhorse of the research centre SAFE (Centre for Accelerator Based Research and Energy Physics), which was established by the University of Oslo in June 2005, merging the nuclear physics group, the nuclear chemistry group, and the energy research group.

The Oslo cyclotron is an MC-35 Scanditronix model delivering pulsed light-ion beams, see Table 3.1 for a list of available beams. The molybdenum data were taken in February and June 2002, the vanadium data in November 2002, and the scandium experiment was carried out in September 2004. In all experiments, a ^{3}He beam was used. For details on the targets, see Table 3.2. In order to prevent pileup in the detectors, the beam current was limited to $\approx 1-2$ nA. The experiments were run for about six days.

Ion	Charge state	Energy range (MeV)	Intensity (μA)
Proton	$^{1}H^{+}$	2-35	100
Deuteron	$^{2}H^{+}$	4-18	100
Helium-3	$^{3}He^{++}$	6-47	50
Helium-4 (α)	$^{4}He^{++}$	8-35	50

Table 3.1: Beams available at the Oslo Cyclotron Laboratory.

Target	Enrichment	Thickness (mg/cm^2)	Reactions	Beam energy (MeV)
$^{45}Sc^{\dagger}$	99.9%	3.4	$^{45}Sc(^{3}He,\alpha\gamma)^{44}Sc$ $^{45}Sc(^{3}He,^{3}He'\gamma)^{45}Sc$	38
$^{51}V^{\dagger}$	99.8%	2.3	$^{51}V(^{3}He,\alpha\gamma)^{50}V$ $^{51}V(^{3}He,^{3}He'\gamma)^{51}V$	30
^{94}Mo	92%	2.7	$^{94}Mo(^{3}He,\alpha\gamma)^{93}Mo$ $^{94}Mo(^{3}He,^{3}He'\gamma)^{94}Mo$	30
^{96}Mo	96.7%	1.9	$^{96}Mo(^{3}He,\alpha\gamma)^{95}Mo$ $^{96}Mo(^{3}He,^{3}He'\gamma)^{96}Mo$	30
^{98}Mo	97.0%	2.0	$^{98}Mo(^{3}He,\alpha\gamma)^{97}Mo$ $^{98}Mo(^{3}He,^{3}He'\gamma)^{98}Mo$	45

† Natural targets.

Table 3.2: Targets and reactions used for the experiments studied in this thesis.

The following nuclei will be studied in this thesis: $^{44,45}Sc$, $^{50,51}V$, and $^{93-98}Mo$. The selected reactions are listed in Table 3.2. The experimental equipment used in the experiment is described in the following sections.

3.2 Experimental setup

The experimental setup at the OCL is shown in Fig. 3.1. The cyclotron is situated in the inner hall, the cyclotron hall, where it delivers the light-ion beam in pulses with a typical frequency of about 8 MHz for ^{3}He ions. The beam from the cyclotron is bent 90° by an analysing magnet into the experimental hall, giving an energy resolution of typically 60 keV of the beam after this magnet[1]. In addition, slits and quadrupole magnets in the beam line allow for collimation and further focusing of the beam, respectively. When the beam reaches the target placed in the centre of the detector array CACTUS (see next section), the diameter of the beam is collimated to about $1-2$ mm.

[1]The analysing magnet is a so-called doubly-focusing magnet, focusing in both the vertical and horizontal direction. The result of ∼60 keV resolution (full width half maximum, FWHM) is obtained with a 38-MeV ^{3}He beam and with 2 mm wide slits in front of the analysing magnet, which has a radius of 1 m.

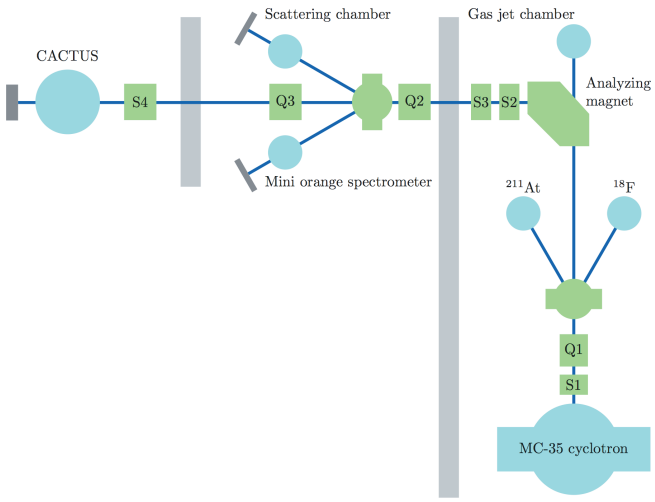

Figure 3.1: Experimental setup at the Oslo Cyclotron Laboratory. The $Q1 \ldots Q4$ are guadrupole magnets, the $S1 \ldots S4$ are slits. The beam dumps marked with ^{211}At and ^{18}F are stations for producing the radioactive isotopes ^{211}At and ^{18}F for medical use and research.

3.2.1 CACTUS

The multi-detector array CACTUS [62] is utilised for measuring particle-γ coincidences. The γ-rays are detected with 28 $5'' \times 5''$ NaI(Tl) detectors mounted on a spherical frame surrounding the target and the particle telescopes, see Fig. 3.2. The NaI(Tl) crystals are collimated with lead collimators, so that their diameter is reduced from 12.7 cm to 7 cm. The solid angle coverage of the collimated NaI(Tl) detectors is estimated to be 17.7% of 4π from $\Omega = \frac{NA}{4\pi R^2}$, where $N = 28$ is the number of detectors, $A = \pi r^2$ is the collimated front area of one detector with radius r = 3.5 cm, and R = 22 cm is the distance of the NaI(Tl) detectors from the target.

The total efficiency was measured to be 15.2% for the 1332-keV γ transition in ^{60}Co. The efficiency was determined by measuring a singles-γ spectrum of a ^{60}Co source with a Ge detector placed in a long distance ($\approx$ 50 cm) from the source. Then, a coincidence requirement was set for the Ge detector and the NaI(Tl)s, so that either the 1173-keV or the 1332-keV transition was measured by the Ge detector or the NaI(Tl)s. The area (counts) reduction in the full-energy peak of the 1173-keV transition of the Ge coincidence spectrum compared to the singles-γ spectrum gave the ef-

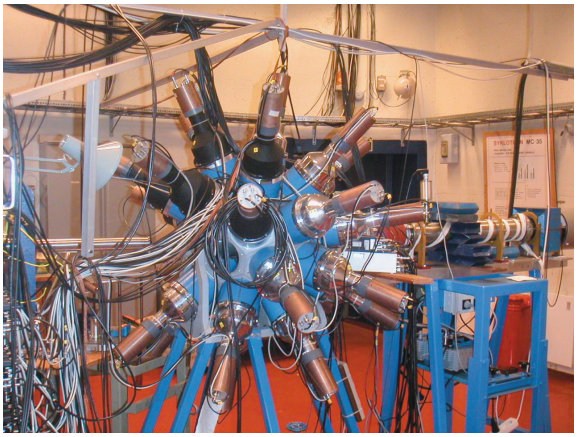

Figure 3.2: The multi-detector array CACTUS.

ficiency of the NaI(Tl)s:

$$\varepsilon_{\mathrm{tot}}^{\mathrm{NaI}}(1332\,\mathrm{keV}) = \frac{N_{\mathrm{coinc}}^{\mathrm{Ge}}(1173\,\mathrm{keV})}{N_{\mathrm{singles}}^{\mathrm{Ge}}(1173\,\mathrm{keV})}, \tag{3.1}$$

where $\varepsilon_{\mathrm{tot}}^{\mathrm{NaI}}$ is the total efficiency of the 28 NaI(Tl)s for $E_\gamma = 1332$ keV, N_{coinc} is the number of counts in the 1173-keV coincidence full-energy peak, and N_{singles} is the number of counts in the 1173-keV singles full-energy peak of the Ge detector.

The resolution of the NaI(Tl) detectors is $\sim$ 7% FWHM for the 1332-keV line. A 2 mm copper absorber is placed in front of each γ detector to suppress X-rays. To reduce crosstalk[2], a 3 mm lateral lead shielding surrounds each NaI(Tl) crystal.

For the runs on the vanadium target, a 60% Ge detector was placed in backward direction in order to monitor the range of spins populated in the (^{3}He,α) and (^{3}He,^{3}He$'$) reactions. It also helped to ensure that the correct nuclei were studied – the good energy resolution allows for the identification of well-known γ transitions in the specific nuclei. The electronics setup allows for three Ge detectors; however, normally only one is used during an experiment.

[2]Crosstalk occurs when a γ ray interacts with one of the detectors and then scatters into another detector. Then, there is a non-negligible probability for the γ ray to be measured by two or more detectors within the detector response time, giving false γ signal.

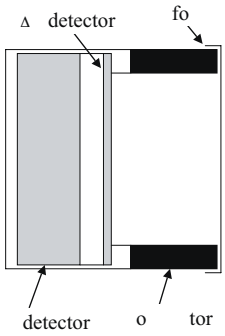

Figure 3.3: Schematic drawing of a Si particle telescope.

The charged particles produced in the nuclear reaction are detected by eight Si $\Delta E - E$ telescopes mounted inside the CACTUS frame. The ΔE counters have a thickness of $\sim$ 140 μm, and the E counters are 1500 μm thick. The particle telescopes are placed 5 cm from the target in the forward direction at an angle of 45° with respect to the beam axis. A 15 μm thick Al foil is placed in front of the particle telescopes in order to stop δ electrons that are emitted from the target foil when the beam is passing through it. The particle detectors were collimated to reduce the uncertainty in the outgoing angle and thereby in the energy of the ejectile. The eight particle telescopes cover 0.2% of 4π when using collimators of 3 mm diameter, as done in the Mo, V, and Sc experiments. The average energy resolution is $\approx 200 - 300$ keV as determined from the FWHM of the elastic ^{3}He peak.

3.2.2 Electronics and data acquisition

At present, the electronics at the OCL is placed partly in the experimental room and partly in the computer room, see Fig. 3.4 and Fig. 3.5. The pulses from the particle and Ge detector(s) are first amplified with preamplifiers mounted close to the detectors, and then sent to timing filter amplifier (TFA) units where fast timing signals are filtered out, amplified and inverted (Fig. 3.4). The signals are also sent to main amplifiers and directly to their corresponding analog-to-digital converters (ADCs). The timing signals are further processed by constant fraction discriminators (CFDs) to obtain essentially walk-free, fast logic signals. For simplicity, the signals

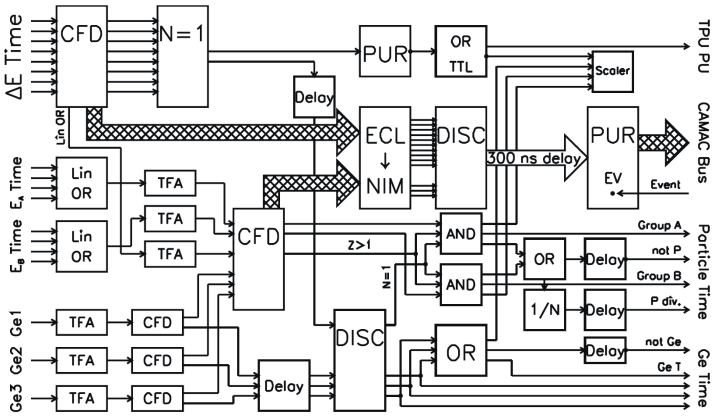

Figure 3.4: Block diagram of the electronics setup in the experimental room, taken from Ref. [63].

from the eight particle end counters are put in groups of four (E_A Time and E_B Time), added by a linear fan in (Lin OR) and processed together (Group A and B). The ΔE detector time signals (ΔE Time) are connected to a multiplicity unit with the setting $N = 1$, which produces a gate signal if one and only one ΔE detector was hit. In addition, a summed, attenuated analog output of the ΔE timing CFD (Lin OR) is fed into a TFA, where it is amplified and then used for a common threshold setting ($Z > 1$). In this way, it is possible, if desired, to suppress events where protons or electrons[3] hit the ΔE detectors.

All the ΔE-detector CFDs are connected to a pile-up rejection module (PUR). This module takes the logic signal from the multiplicity unit and stretches it for ≈ 1 µs, and if another pulse arrives within this time interval, the PUR gives an inverted logic signal to indicate a pile-up event. Then the pile-up signal is sent to a VME trigger pattern unit (TPU), where the event is marked as pileup.

The coincidence events of the ΔE and E detectors are made by requiring three conditions:

1. Exactly one ΔE detector is hit.

2. The signal of the ΔE detector is larger than the common threshold setting ($Z = 1$).

[3]Fast electrons and protons with $Z = 1$ deposit only a small fraction of their energy in the ΔE counters.

3. At least one E detector is hit.

This is done by a coincidence unit (AND) checking whether the E detector CFD signal, the multiplicity unit signal, and the $Z > 1$ CFD signal are in coincidence with each other. Unfortunately, there is neither a hardware condition that the ΔE and E detector of the same particle telescope are hit, nor that only one E detector gave a signal. However, since the particle multiplicity and the beam current are relatively low, this does not introduce severe problems, and can also be checked during offline data sorting.

A scaler serves as a counter for several unit signals, such as the coincidence rate of the particle telescopes and the summed rate of the Ge detectors. Since the elastically scattered ^{3}He particles produce a high count rate due to the large Rutherford cross section, every other event is rejected with a $(1/N)$ module with the setting $N = 2$ unless a γ-ray detector is hit; thus, the particle singles spectrum is divided by two (shown as 'P div.' output in Fig. 3.4).

The electronics setup in the computer room is displayed in Fig. 3.5. The timing signals from the NaI(Tl) detectors (NaI Time) are processed by CFD units. The coincidence of the signals from the particle telescopes and the γ-ray detectors is first tested with a gated discriminator (DISC) shown in the upper part of Fig. 3.5. The DISC is vetoed unless a particle counter gives a signal. Then, if a coincidence is measured, a logic signal is sent to start a time-to-digital converter (TDC). Another branch, delayed by 200 ns, is used to stop the TDC. The gate generators (GG) connected to the DISC create a gate signal for the analog-to-digital converters (ADC) for the NaI(Tl) detectors (ADC NaI) and the Ge detectors (ADC Ge1/2/3/T). The other logic units connected to the DISC are used to (i) identify which particle-telescope group is in coincidence with the γ ray(s) (NaI OR, Ge OR, γ OR, γ+p OR, A OR (AND), B OR (AND), Delay), and subsequently send a gate signal to open the particle-telescope ADC, (ii) start the Ge-detector time-to-amplitude converter (TAC) which, with the ADC GeT unit, works as a TDC (Ge OR), and (iii) set flags in the VME trigger pattern units (TPU), which control the readout of the digitized data.

In Table 3.3 all the hit patterns for the TPUs are listed. TPU1 handles the particle telescopes and the Ges, while TPU2 and TPU3 deal with the NaI(Tl) detectors. The virtual TPU4 is not a real module, but is created by the sorting program (see next two sections) in order to show in which detectors pile-up events occured. For simplicity, the control of the NIM-ADCs by VME-ADC controllers, and the control of the CAMAC crate by a CAMAC-branch driver are not shown in Fig. 3.5. The VME crate ac-

Bit #	TPU 1	TPU 2	TPU 3	TPU 4 (virtual, for pile up)
0	Group A	NaI(Tl) 1	NaI(Tl) 17	ΔE 1
1	Singles	NaI(Tl) 2	NaI(Tl) 18	ΔE 2
2	Group B	NaI(Tl) 3	NaI(Tl) 19	ΔE 3
3	Coincidence	NaI(Tl) 4	NaI(Tl) 20	ΔE 4
4	Ge 1	NaI(Tl) 5	NaI(Tl) 21	ΔE 5
5		NaI(Tl) 6	NaI(Tl) 22	ΔE 6
6	Ge 2	NaI(Tl) 7	NaI(Tl) 23	ΔE 7
7		NaI(Tl) 8	NaI(Tl) 24	ΔE 8
8	Ge 3	NaI(Tl) 9	NaI(Tl) 25	Ge 1
9		NaI(Tl) 10	NaI(Tl) 26	Ge 2
10	Ge time	NaI(Tl) 11	NaI(Tl) 27	Ge 3
11		NaI(Tl) 12	NaI(Tl) 28	
12		NaI(Tl) 13	NaI(Tl) 29	
13		NaI(Tl) 14	NaI(Tl) 30	
14		NaI(Tl) 15	NaI(Tl) 31	E_A
15		NaI(Tl) 16	NaI(Tl) 32	E_B

Table 3.3: Hit patterns for the TPUs.

commodates connections to the SUN-Sparc station via a BIT3 Sun Sbus to VMEbus interface.

Each event is constructed on an event-by-event basis by the program Eventbuilder+ [64], running on a CES RIO2 single board processor in the VME crate with a PowerPC 604r @ 300 MHz CPU running LynxOS. The event structure is similar to that of Fig. 4.2 in Ref. [64]; the event starts with a 16-bit word, were bits 12–15 are set to indicate the start of a new event. The bits 0–11 describe the total event length. The next two words denote which TPU is read and its pattern word, respectively. The follow words contain the data (energy, time) of the corresponding detector(s). Then the next TPU is read and so on, until all information of this particular event is recorded. The events are then put in buffers with a length of 32768 words. When a buffer is full, it is transferred to the Sun SPARC computer, where the data acquisition program Sirius+ [64] writes the event buffer to disk. While waiting for buffers, the program sorts events on-line for monitoring the experiment.

The hit patterns of the TPUs displayed in Table 3.3 indicate whether the corresponding detector has data. When sorting the data files off-line with the program Offline+ [65], an event matrix is generated so that the user can access energies and times from this matrix in the sorting user routine.

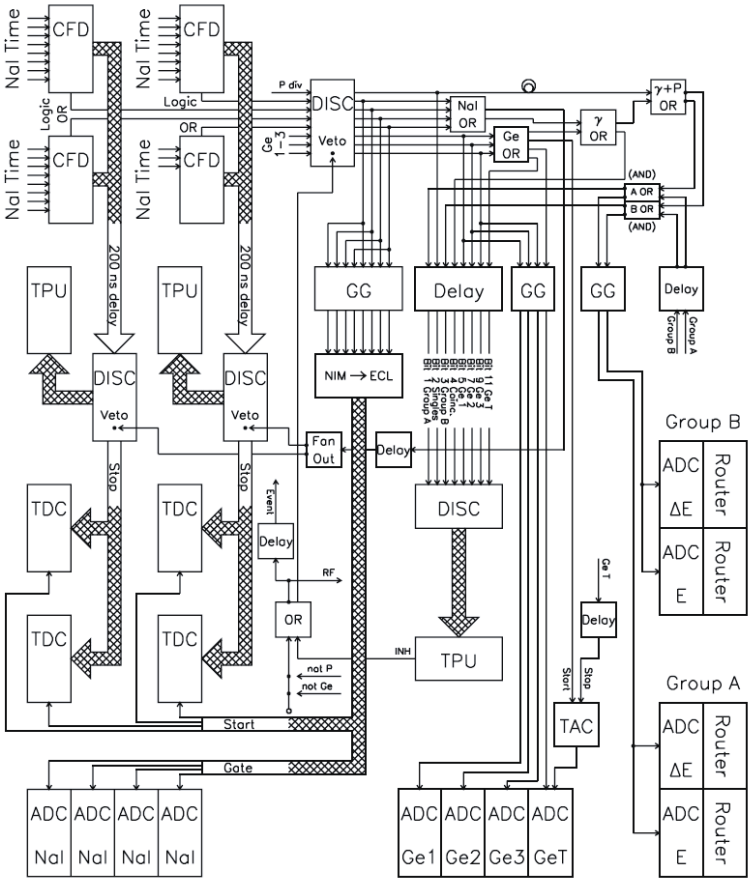

Figure 3.5: Block diagram of the electronics setup in the computer room, taken from Ref. [63].

3.3 Data analysis

In this section, the data analysis applied on the event files will be briefly discussed, as well as the techniques involved to obtain a coincidence matrix with γ-decay spectra for each given excitation energy.

3.3.1 Selected reactions

As previously described, the ^{3}He beam energy used for the experiments discussed here is between $30 - 45$ MeV. Letting these ^{3}He ions impinge on the targets, several reaction channels are opened, such as (^{3}He,xnγ), (^{3}He,dγ), (^{3}He,xn$\alpha\gamma$), and (^{3}He,^{3}He$'\gamma$). The reactions of interest for this study were the inelastic scattering (^{3}He,^{3}He$'\gamma$) and the (^{3}He,$\alpha\gamma$) pick-up reaction as shown in Table 3.2. As there are no neutron detectors present in the experimental setup, and it is necessary to measure all the ejectiles' energies in order to precisely determine the initial excitation energy of the target nucleus, the highest excitation energy for which the γ spectra can be used is the neutron binding energy B_n. If a proton is emitted, the proton binding energy B_p plus the Coulomb barrier is the excitation limit. In Table 3.4, the proton and neutron binding energies for all the nuclei studied in this work are shown, together with the Coulomb barrier for proton emission and the reaction Q value in the case where the nuclei are populated through the (^{3}He,$\alpha\gamma$) reaction. The Coulomb barrier for the proton is given by

$$U_{\text{Coul}} = \frac{e^2}{4\pi\epsilon_0}\frac{Z_{\text{p}}Z_{\text{target}}}{R_{\text{p}} + R_{\text{target}}}, \tag{3.2}$$

where the factor $e^2/4\pi\epsilon_0 = 1.44\,\text{MeV}\cdot\text{fm}$, the sum of the radii $R_{\text{p}} + R_{\text{target}} = r_0(A_{\text{p}}^{1/3} + A_{\text{target}}^{1/3})$ with $r_0 \approx 1.25$ fm, and Z_{p}, Z_{target} are the electric charge of the proton and the target nucleus, respectively.

The maximum angular momentum transfer ℓ_{max} possible in the reactions can roughly be estimated using the classical expression

$$\left|\vec{\ell}\right| = |\vec{r} \times \vec{p}| = rmv\sin\theta. \tag{3.3}$$

For $\theta = 90°$, we have

$$\ell = R_{\text{target}} m_{^3\text{He}} v = r_0 A_{\text{target}}^{1/3} m_{^3\text{He}} \sqrt{\frac{2E_k}{m_{^3\text{He}}}}, \tag{3.4}$$

where the relation

$$E_k = \frac{1}{2}mv^2 \tag{3.5}$$

Nucleus	I^π	B_p (MeV)	B_n (MeV)	Coulomb barrier (MeV)	Q value (MeV)
^{44}Sc	2^+	6.696	9.700	5.34	9.255
^{45}Sc	$7/2^-$	6.889	11.32	5.31	-
^{50}V	6^+	7.949	9.332	5.66	9.526
^{51}V	$7/2^-$	8.061	11.05	5.63	-
^{93}Mo	$5/2^+$	7.643	8.070	8.75	10.90
^{94}Mo	0^+	8.490	9.678	8.72	-
^{95}Mo	$5/2^+$	8.632	7.369	8.70	11.42
^{96}Mo	0^+	9.298	9.154	8.67	-
^{97}Mo	$5/2^+$	9.226	6.821	8.65	11.94
^{98}Mo	0^+	9.794	8.643	8.62	-

Table 3.4: Neutron and proton binding energies, ground-state spin/parity, Coulomb barriers, and Q values for the nuclei under study.

for the kinetic energy E_k of the ^{3}He projectile has been utilized. Using $r_0 \approx 1.25$ fm, $A_{\text{target}} = 98$, $E_k = 45$ MeV, $m_{^3\text{He}} = 2809.41$ MeV$/c^2$ and $\hbar c = 192.329$ MeV $\cdot$ fm gives

$$\ell_{\max} \approx 15\hbar \tag{3.6}$$

for the target nucleus ^{98}Mo. Of course, to get a more precise estimate for the expected spin window populated, one should perform more realistic reaction calculations based on reaction theory such as the distorted wave Born approximation (DWBA, see [1, 66]), taking into account the quantum nature of the impinging ion and the target nucleus, and also the geometry, as the particle telescopes are placed 45° with respect to the beam axis. Previous experiments [67] and DWBA calculations [68] have shown that for the (^{3}He,α) reaction, the pick-up of neutrons with high ℓ-values are preferred. For the nuclei Sc, V, and Mo, the spin range of states populated by the direct reactions is typically $2\hbar \leq I \leq 6\hbar$.

3.3.2 Coincidence technique

As displayed in Figs. 3.4 and 3.5, the electronics setup consists of a *fast* branch that treats the timing information, and a *slow* branch that ensures the best possible handling of the energy information [69]. The time between the detection of a particle and one or more γ-rays is registered by TDCs for the NaI(Tl) detectors and a TAC plus an ADC for the Ge detector. By setting gates on the prompt peak in the measured time spectra when

sorting the data offline, the true coincident events were obtained, i.e. the particle and the γ-rays are detected within a narrow time interval. The present electronics setup has a time window of 200 ns, which means that the master gate signal set by the particle (start of the TDCs/TAC) has a duration of 200 ns.

Figure 3.6 shows the time spectrum from the ^{51}V(^{3}He,$\alpha\gamma$)^{50}V, and the gates chosen for the random background (left) and the prompt peak (right). The time resolution is determined by the FWHM of the prompt peak, which is in this case about 17 ns. The gated area of the peak to the left gives the number of random coincidences, and in addition the events where γ-rays from a reaction stemming from one beam burst are detected in coincidence with particles from a reaction produced by the next beam burst. Roughly, the true number of coincidences can be obtained by subtracting the events in the random peak from the prompt peak. Therefore, during the offline data sorting, events that fall into the random gate will be decremented and events in the prompt gate will be incremented, while everything else is rejected.

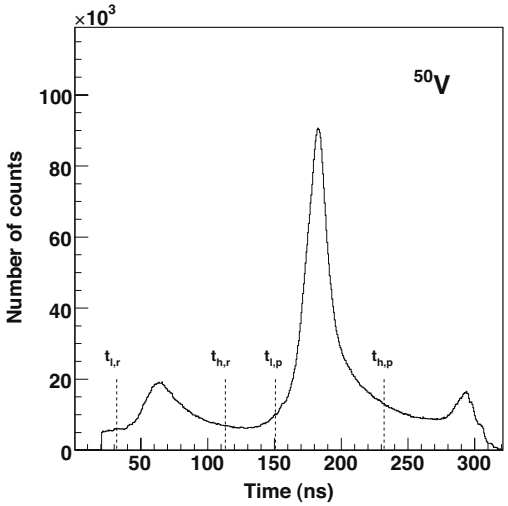

Figure 3.6: The time spectrum of ^{50}V. The dashed lines indicate lower ($t_{l,r}$, $t_{l,p}$) and upper ($t_{h,r}$, $t_{h,p}$) gates on the random and prompt peak, respectively.

3.3.3 Particle–γ matrix

In order to obtain the particle energy vs. γ-ray energy matrix, each individual particle telescope and NaI(Tl) detector is calibrated with a linear calibration

$$E = a_0 + a_1 \cdot \mathrm{ch}, \tag{3.7}$$

where E is the energy, a_0 is the constant shift, a_1 is the dispersion and ch is the channel number in the spectrum. When all detectors are properly calibrated, one can add the data of all the particle telescopes together, and likewise the NaI(Tl) spectra.

The particle telescopes allow for particle identification by utilizing the fact that the energy loss of a charged particle per unit length in a medium is a function of the charge and the mass of the penetrating particle according to the Bethe-Bloch formula [69]. The penetration depth or range as a function of the particle's kinetic energy differs for each charged particle due to their different charge and mass numbers. A given particle will therefore lose a different amount of its energy in the ΔE and E detectors as a function of its total kinetic energy. Such a plot of the energy deposited in the ΔE detector vs. the energy deposited in the E detector is shown in Fig. 3.7, with characteristic banana-shaped curves for each type of particle.

The particle-identification technique described above makes it possible to gate on a specific particle type utilizing its unique range curve in the Si detectors. By gating on the ^{3}He and α particles event-by-event in the offline sorting procedure in addition to the gates on the time spectrum, the ^{3}He–γ and α–γ coincidence events can be extracted. Figure 3.8 shows the α–γ coincidence matrix of the ^{45}Sc(^{3}He,$\alpha\gamma$)^{44}Sc reaction.

The α–γ coincidence matrix in Fig. 3.8 displays characteristic features such as the diagonal where the excitation energy equals the γ-ray energy $E = E_\gamma$. The strong population of yrast states in many excitation-energy bins is shown as intense, vertical lines in the matrix at low γ-ray energy. In the region of excitation energies around $8 - 9$ MeV, the γ-ray multiplicity is seen to be drastically reduced. In this region, the excitation energy is high enough so that proton/neutron emission starts to compete with γ-ray emission, and the nucleus with $A - 1$ is populated.

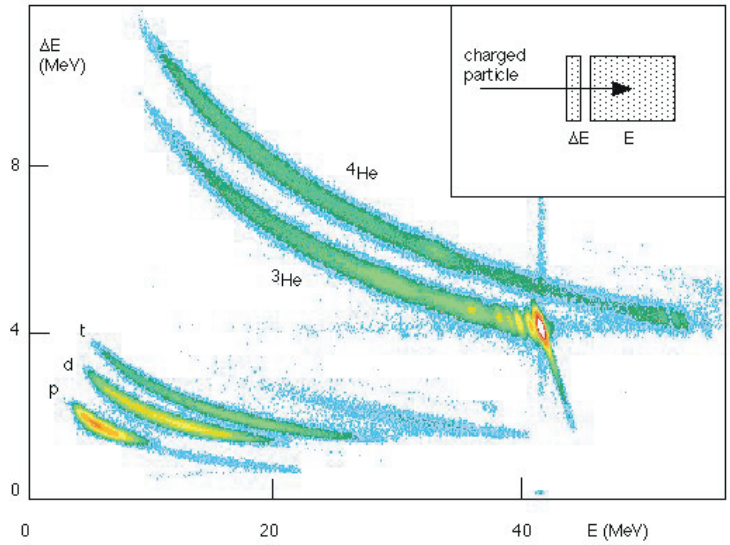

Figure 3.7: Identification of the ejectiles (bananas) by plotting the energy deposited in the thin ΔE detector versus the energy deposited in the thick E detector of the Si particle telescopes (insert).

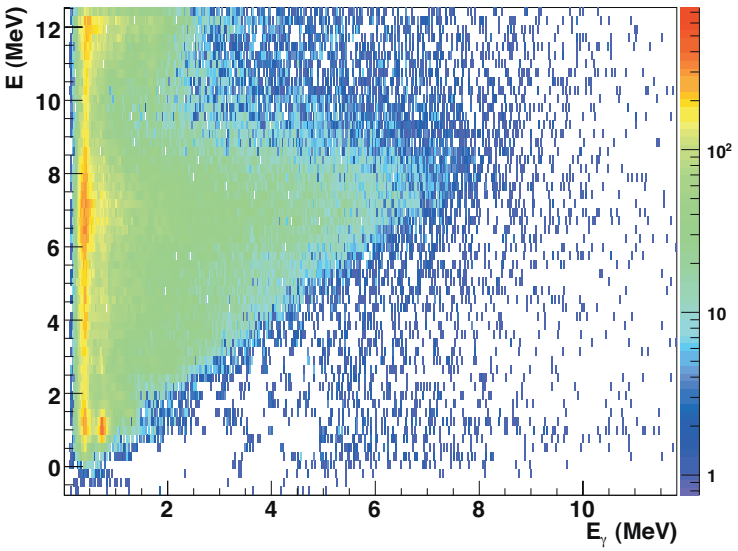

Figure 3.8: Alpha–γ coincidence matrix of ^{44}Sc. The energy of the α particle is transformed into excitation energy E of the residual nucleus using the reaction kinematics and the Q-value.

Chapter 4

The Oslo method

Based on the particle-γ coincidence matrix that is obtained by tagging the measured γ rays with the corresponding particle energy, the Oslo group has developed a method to unfold the γ-ray spectra by means of the response functions of the CACTUS array. In this way, the γ-ray spectra for each excitation energy are corrected for the single- and double escape peak, the annihilation peak, the Compton events, and the detector efficiency [2]. From the unfolded γ-ray spectra, the first γ-rays emitted in the decay cascades from each excitation energy are extracted utilizing a subtraction procedure called the 'first-generation method' [3]. This matrix of primary γ-rays contains information on the level density and the average γ-ray transition probability, which are extracted simultaneously through an iterative procedure with a global fit to the experimental first-generation matrix [4]. Together, these three methods are called the Oslo method.

4.1 Unfolding the γ-ray spectra

The response function of a γ-ray detector depends on the various interactions with matter that the photons can undertake: Compton scattering, photoelectric absorption, and pair production. Ideally, the original γ-ray is fully absorbed and is found in the full-energy peak in the γ-ray spectrum. However, since Compton-scattered photons and one or both of the annihilation photons can escape from the detector and thus deposit only part of the full energy, it is necessary to correct the observed γ-ray spectra for such incompletely detected photons. Additional background from backscattered annihilation and Compton γ-rays in the surroundings of the experimental setup give rise to peak structures at 511 and $\approx$ 200 keV, respectively.

To obtain proper γ-ray spectra, one in principle needs to know the response of the detector for all incident γ-ray energies. In practice, however, one is limited to several well-known γ lines from calibration sources such as ^{152}Eu, ^{60}Co, and ^{137}Cs, and in addition γ lines from in-beam experiments. It is therefore mandatory to choose an appropriate procedure to interpolate between the response functions of the monoenergetic γ-rays to get the response function of all γ energies. The technique used here is explained in detail in Ref. [2], where a folding iteration method called the Compton subtraction method is applied in order to construct full-energy γ spectra. A brief outline of the method is given in the following.

First, the detector response functions $R(E, E_\gamma)$, where E is the actual amount of energy deposited in the detector, are established for available incident γ-ray energies E_γ. In total, ten response functions have been measured for monoenergetic γ lines ranging from 122 to 15 110 keV [2]. These spectra are the basis for interpolating to intermediate full energy γ-ray peaks. This interpolation is easily done for the peak structures, that is, the full energy (f), single escape (s), double escape (d), and annihilation (a) peaks, by adding a Gaussian distribution at the interpolated peak position with proper intensity and width. However, the interpolation of the Compton background is more complicated, as the observed Compton background response functions have different maximum energy depending on their respective full energy values. Therefore, the interpolation operates along a set of curves forming a fan, connecting the same channels in the lower end and the highest channels in the upper end of the spectra, see Fig. 4.1. A γ-ray that is scattered at an angle θ transfers an energy E to the electron as given by

$$E = E_\gamma - \frac{E_\gamma}{1 + \frac{E_\gamma}{m_e c^2}(1 - \cos\theta)}, \tag{4.1}$$

where m_e is the electron mass and c is the speed of light. As a reasonable approach, the Compton background is thus interpolated between channels having the same Compton scattering angle θ (see Fig. 4.1).

Having the appropriate response matrix $\mathbf{R}$ at hand, the unfolding procedure can be applied on the experimental γ-ray spectra. The folding iteration method takes advantage of the fact that folding is easy and fast to perform. Each matrix element R_{ij} of the response matrix $\mathbf{R}$ is defined as the response in channel i when the detector is hit by γ-rays with an energy corresponding to channel j. For each incident γ-ray energy channel j, the response function is normalized so that $\sum_i R_{ij} = 1$. The folding is then

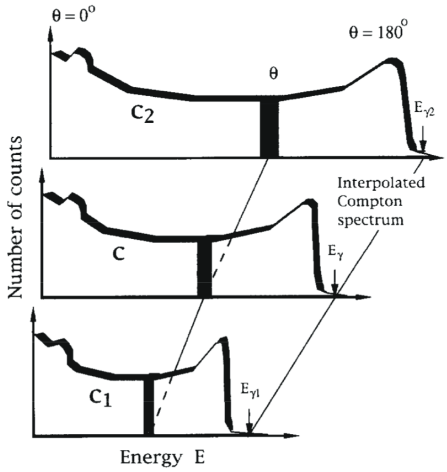

Figure 4.1: The interpolation of the Compton part of the measured response functions c_1 and c_2, illustrating the increase of $\Delta\theta$ with the full energy E_γ.

expressed as

$$f = \mathbf{R}u, \tag{4.2}$$

or, explicitly,

$$\begin{pmatrix} f_1 \\ f_2 \\ \vdots \\ f_N \end{pmatrix} = \begin{pmatrix} R_{11} & R_{12} & \dots & R_{1N} \\ R_{21} & R_{22} & \dots & R_{2N} \\ \vdots & \vdots & \dots & \vdots \\ R_{N1} & R_{N2} & \dots & R_{NN} \end{pmatrix} \begin{pmatrix} u_1 \\ u_2 \\ \vdots \\ u_N \end{pmatrix}. \tag{4.3}$$

Here, f and u represent the folded and unfolded spectra, respectively. Thus by obtaining better and better trial spectra for u, those trial functions can be folded with the corresponding response functions and compared with the observed γ spectrum, hereby denoted r. In practice, the folding iteration method is carried out as follows:

1. As the first trial function u^0 for the unfolded spectrum, the observed spectrum r is used:
$$u^0 = r. \tag{4.4}$$

2. The first folded spectrum f^0 is then calculated,
$$f^0 = \mathbf{R}u^0. \tag{4.5}$$

3. The next trial function u^1 is obtained by adding the difference spectrum $r - f^0$ as a correction to the original trial function u^0:

$$u^1 = u^0 + (r - f^0). \tag{4.6}$$

4. The new trial function u^1 is folded again to get the next f^1, which again is used to generate the next trial function:

$$u^2 = u^1 + (r - f^1), \tag{4.7}$$

and so on until $f^i \sim r$, where i is the iteration index.

Typically, ten iterations ($i = 10$) are sufficient to get a folded spectrum that agrees with the observed spectrum within the experimental uncertainties. However, the obtained unfolded spectrum $u^{10} = u$ exhibits strong oscillations and fine structures, which give artificially a better resolution of u than the experimental resolution. This problem is mended by the Compton subtraction method [2].

The starting point for the Compton subtraction method is the unfolded spectrum u resulting from the folding iteration method as described above, hereby denoted u_0. This spectrum is used to create the expected contributions from the full energy u_f, single escape u_s, double escape u_d, and annihilation u_a part of the original, observed spectrum:

$$u_\mathrm{f}(i) = p_\mathrm{f}(i)u_0(i), \tag{4.8}$$
$$u_\mathrm{s}(i - i_{511}) = p_\mathrm{s}(i)u_0(i), \tag{4.9}$$
$$u_\mathrm{d}(i - i_{1022}) = p_\mathrm{d}(i)u_0(i), \tag{4.10}$$
$$u_\mathrm{a}(i_{511}) = \sum_i p_\mathrm{a}(i)u_0(i), \tag{4.11}$$

where i_{511} and i_{1022} represent the channels with energies 511 and 1022 keV, respectively. The factors $p_\mathrm{f}(i)$, $p_\mathrm{s}(i)$, $p_\mathrm{d}(i)$, and $p_\mathrm{a}(i)$ are the probabilities for an event in channel i to be a photo peak, single escape, double escape, or annihilation event, respectively (see Table 1 in Ref. [2]). The probabilities are normalized so that

$$\sum_i p_\mathrm{f}(i) + p_\mathrm{s}(i) + p_\mathrm{d}(i) + p_\mathrm{a}(i) + p_\mathrm{c}(i) = 1, \tag{4.12}$$

where $p_\mathrm{c}(i)$ is the probability for a Compton event in channel i.

The u_a spectrum, originally with all its counts in channel i_{511}, must be smoothed with the experimental resolution denoted 1.0 FWHM in order

to get the energy resolution of the observed spectrum. The energy resolution of the spectra u_f, u_s, and u_d is determined by the resolution of the observed spectrum (1.0 FWHM) and the response matrix (0.5 FHWM) giving[1] $\sqrt{1.0^2 - 0.5^2}$ FWHM $= 0.87$ FWHM. Therefore, an additional smoothing of 0.5 FWHM is done to get a spectrum with the experimental resolution of 1.0 FWHM: $\sqrt{0.87^2 + 0.5^2}$ FWHM ≈ 1.0 FWHM.

The Compton background spectrum[2] $c(i)$ can now be found by subtracting the components u_f, u_s, u_d, and u_a from the experimentally observed spectrum $r(i)$:

$$c(i) = r(i) - v(i), \tag{4.13}$$

where

$$v(i) = u_f + u_s + u_d + u_a. \tag{4.14}$$

The extracted Compton spectrum $c(i)$ displays strong oscillations of the same order as the experimental spectrum $r(i)$. To be able to preserve the experimental, statistical fluctuations, an additional, rather strong smoothing of 1.0 FWHM is applied on the spectrum $c(i)$, justified by the fact that this spectrum should be a *s*lowly varying function of energy. The total smoothing of $c(i)$ is then $\sqrt{2}$ FWHM.

To obtain the unfolded energy spectrum u_{unf} of full-energy peaks, the smoothed Compton spectrum c and the peaks u_s, u_d, and u_a are subtracted from the observed spectrum r:

$$u_{unf}(i) = r(i) - c(i) - u_s(i - i_{511}) - u_d(i - i_{1022}) - u_a(i_{511}). \tag{4.15}$$

Finally, the true γ-ray energy distribution is calculated, correcting u_{unf} for the full energy probability p_f and the energy-dependent total γ-ray detection efficiency ϵ_{tot}:

$$U_{unf}(i) = \frac{u_{unf}(i)}{p_f(i)\epsilon_{tot}(i)}. \tag{4.16}$$

Here, ϵ_{tot} is taken from Table 1 in Ref. [2]. In addition, ϵ_{tot} is multiplied with the energy-dependent cutoff function reflecting the individual detector's discriminator level. Typically, the experimental energy threshold is about 100-200 keV with a width of ≈ 100 keV.

Figure 4.2 shows an example of the resulting α–γ coincidence matrix of ^{44}Sc, where all γ-ray spectra for each excitation-energy bin are unfolded

[1] Assuming that the spectra f, r, and u follow a Gaussian behavior, we have $(\delta f)^2 = (\delta r)^2 + (\delta u)^2$, giving $\delta u = \sqrt{(\delta f)^2 - (\delta r)^2}$.

[2] This Compton spectrum also contains the backscattering peak at ≈ 200 keV stemming from Compton backscattered γ-rays of the surroundings, in addition to other background events such as X-rays.

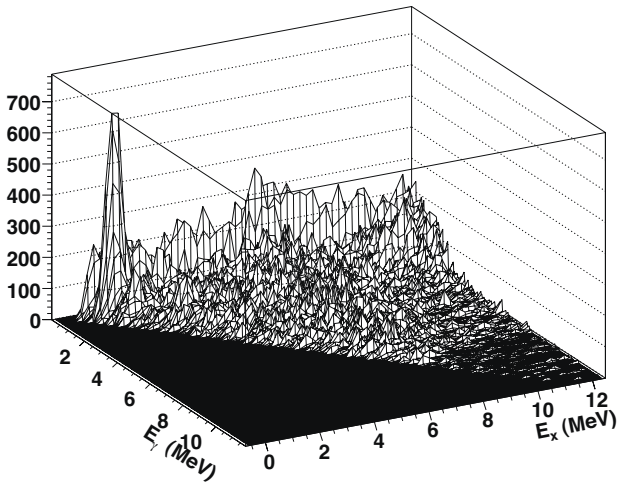

Figure 4.2: Unfolded α–γ coincidence matrix of ^{44}Sc.

using the above-described method. A fraction of the matrix is displayed in Fig. 4.3, where a projection of the γ-ray spectra has been performed for excitation energies between 5.5–6.5 MeV. As is seen from Fig. 4.3 by comparing the original and the folded spectrum, the unfolding procedure works very well.

4.2 Distribution of first-generation γ rays

In general, the γ decay from highly excited states involves a cascade of transitions. The measured γ spectra will contain contributions from all decay steps, since the γ decay in the quasi-continuum is generally very fast ($\approx 10^{-15}$ s) and as no timing technique is able to determine the order of the γ-rays that belonged to a specific cascade. As the generations of γ rays are not well separated in energy either, it is difficult to get hold of the distribution of primary γ-rays in this excitation-energy region.

The nuclear physics group at the OCL has developed a subtraction method to extract the primary (first-generation) γ-rays from the quasi-continuum γ-ray spectra measured for each excitation-energy bin. The method is described in detail in Ref. [3], and its main features will be

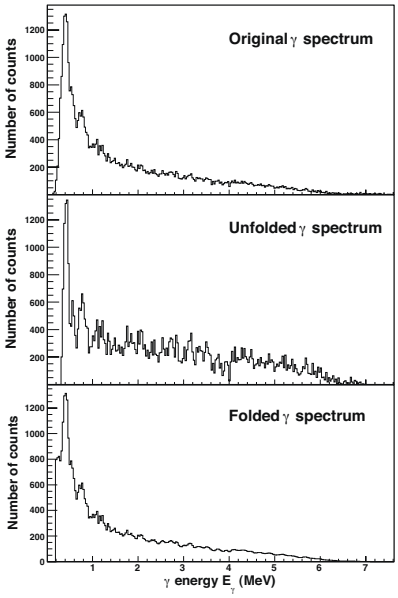

Figure 4.3: Original (top), unfolded (middle) and folded γ spectrum of ^{44}Sc for excitation energy between $5.5 - 6.5$ MeV.

sketched here.

The main assumption of the first-generation method is that the γ decay from any excitation-energy bin is independent on how the nucleus was excited to this bin. In other words, the decay routes are the same whether they were initiated directly by the nuclear reaction or by γ decay from higher-lying states. This assumption is automatically fulfilled when states have the same cross section to be populated by the two processes, since γ branching ratios are properties of the levels themselves. Even if different states are populated, the assumption is still valid for statistical γ decay, which only depends on the γ-ray energy and the number of accessible final states. Here, in the region of high level density, the nucleus seems to attain a compound-like system before emitting γ-rays even though the direct reactions (^{3}He,α) and (^{3}He,^{3}He$'$) are utilized. This is because the reaction time, and thus the time it takes to create a complete compound state, is $\approx 10^{-18}$s, while the typical life time of states in the quasi-continuum is $\approx 10^{-15}$s. Therefore, it is reasonable to assume that the nucleus has thermalized prior to γ decay.

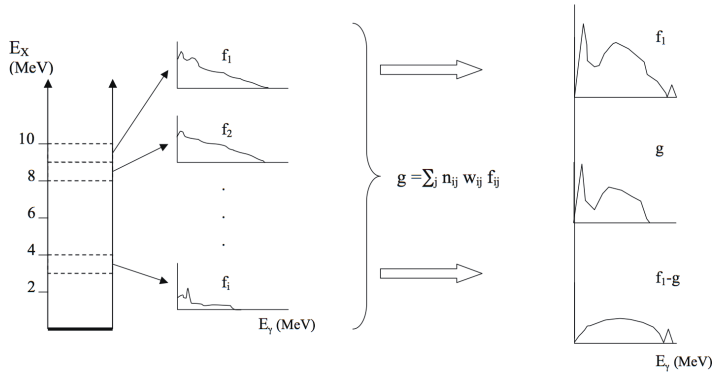

Figure 4.4: Illustration of the principle of the first-generation method (see text).

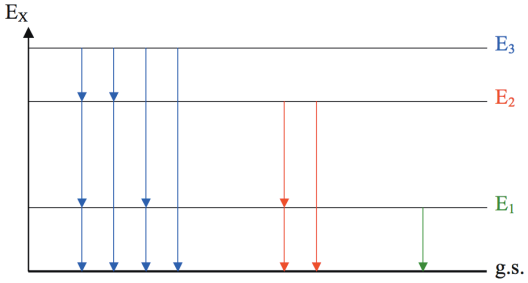

Figure 4.5: A hypothetical γ-decay cascade. The first-generation γ rays from level E_3 can be obtained by subtracting the γ spectra from the levels E_2 and E_1.

The method is illustrated in Fig. 4.4. For each excitation-energy bin i (typically $120 - 240$ keV wide), a γ-ray spectrum f_i is projected out from the total particle–γ coincidence matrix, which is generated as described in Sec. 3.3.3 and unfolded as explained in Sec. 4.1. The unfolded spectra f_i are made of all generations of γ rays from all possible cascades decaying from the excited levels within the bin i. Now, we utilize the fact that the spectra $f_{j<i}$ for all the underlying energy bins j contain the same γ transitions as f_i *except* the first γ rays emitted, since they will bring the nucleus from the states in bin i to underlying states in the energy bins j. This is shown for one specific, hypothetical cascade in Fig. 4.5, where it is easily seen that by subtracting the γ spectra from the levels E_2 and E_1, the first-generation spectrum of level E_3 is found. The picture of Fig. 4.5 is of course oversimplified. In reality, one has to take into account the different cross

sections for populating the levels in the various energy bins i and also the different intensities (branching ratios) of the primary γs. Therefore, the first-generation spectrum h_i is found by

$$h_i = f_i - g_i, \tag{4.17}$$

where g_i is a weighted sum of all spectra

$$g_i = n_{i1}w_{i1}f_1 + n_{i2}w_{i2}f_2 + \ldots + n_{ij}w_{ij}f_j = \sum_j n_{ij}w_{ij}f_j. \tag{4.18}$$

Here, the unknown coefficients w_{ij} (with $\sum_j w_{ij} = 1$) represent the probability of the decay from bin i to bin j. In other words, w_{ij} is the weighting coefficient or branching ratio of each primary γ-ray depopulating level i. In this sense, the w_{ij} values correspond directly to the first-generation spectrum h_i.

The coefficients n_{ij} are correcting factors for the different cross sections of populating level i and the underlying levels j, and are determined so that the total area of each spectrum f_i multiplied by n_{ij} corresponds to the same number of cascades. This can be done in two ways [3]:

- Singles normalization. The singles-particle cross section is proportional to the number of populated states and thus to the number of decay cascades. We denote the number of counts measured for bin i and j in the singles spectrum S_i and S_j, respectively. The normalization factor n_{ij} that should be applied to the spectrum f_j is then given by

$$n_{ij} = \frac{S_j}{S_i}. \tag{4.19}$$

- Multiplicity normalization. The average γ-ray multiplicity $\langle M \rangle$ can be obtained in the following way [70]: Assume an N-fold population of an excited level E. The decay from this level will result in N γ-ray cascades, where the ith cascade contains M_i γ rays. The average γ-ray energy $\langle E_\gamma \rangle$is equal to the total energy carried by the γ rays divided by the total number of γ rays:

$$\langle E_\gamma \rangle = N \cdot \frac{E}{\sum_{i=1}^{N} M_i} = \frac{E}{\frac{1}{N}\sum_{i=1}^{N} M_i} = \frac{E}{\langle M \rangle}. \tag{4.20}$$

  Then, the average multiplicity is simply given by

$$\langle M \rangle = \frac{E}{\langle E_\gamma \rangle}. \tag{4.21}$$

The average γ-ray multiplicity $\langle M_i \rangle$ can thus easily be calculated for each excitation-energy bin i. Let the area (or total number of counts) in spectrum f_i be denoted by $A(f_i)$. Then the singles particle cross section S_i is proportional to the ratio $A(f_i)/\langle M_i \rangle$, and the normalization coefficient n_{ij} that should be applied to bin i when subtracting bin j is

$$n_{ij} = \frac{A(f_i)/\langle M_i \rangle}{A(f_j)/\langle M_j \rangle} = \frac{\langle M_j \rangle A(f_i)}{\langle M_i \rangle A(f_j)}. \tag{4.22}$$

In order to choose between the two normalization methods, one needs to consider the actual experimental conditions. For example, if the nucleus studied has an isomeric state that has a longer life time than the time range of the TDCs, the γ decay from this state will not be measured in coincidence with the outgoing particle. This was the case for the nucleus ^{44}Sc, which has an isomer at $E = 271.13$ keV with a half-life of 58.6 hours [26]. Therefore, the multiplicity normalization was applied for the Sc nuclei. In general, the two normalization methods give very similar results.

In cases where the multiplicity is well determined, an area consistency check can be applied to Eq. 4.17. Assume that a small correction has to be introduced by substituting g_i by αg_i, where α is close to unity. The area of the first-generation γ spectrum is then

$$A(h_i) = A(f_i) - \alpha A(g_i), \tag{4.23}$$

and corresponds to a γ-ray multiplicity of one unit. Since the number of primary γ rays in the spectrum f_i equals $A(f_i)/\langle M_i \rangle$, $A(h_i)$ is also given by

$$A(h_i) = A(f_i)/\langle M_i \rangle. \tag{4.24}$$

Combining Eqs. (4.23) and (4.24) yields

$$\alpha = (1 - 1/\langle M_i \rangle)\frac{A(f_i)}{A(g_i)}. \tag{4.25}$$

The α parameter can be varied to get the best agreement of the areas $A(h_i)$, $A(f_i)$ and $A(g_i)$ within the following restriction: $\alpha = 1.00 \pm 0.15$; that is, the correction should not exceed 15%. If a greater correction is necessary, then improved weighting functions w_{ij} should be determined instead.

As mentioned before, the weighting coefficients w_{ij} correspond directly to the first-generation spectrum h_i, and this close relationship makes it possible to determine w_{ij} (and thus h_i) through a fast converging iteration procedure [3]:

1. Apply a trial function w_{ij}.
2. Deduce h_i.
3. Transform h_i to w_{ij} by giving h_i the same energy calibration as w_{ij}, and normalizing the area of h_i to unity.
4. If w_{ij}(new) $\approx w_{ij}$(old), convergence is reached and the procedure is finished. Otherwise restart from step 2.

Tests of the convergence properties of the procedure have shown that excellent agreement is achieved between the exact solution (from simulated spectra) and the trial function w_{ij} already after three iterations [3]. Usually, about 10 iterations are performed on experimental spectra.

To demonstrate how well the first-generation procedure works, Fig. 4.6 shows the total, unfolded γ spectrum, the second and higher generations γ-ray spectrum and the first-generation spectrum of ^{45}Sc for excitation energy between $E = 5.5 - 6.5$ MeV. The first-generation spectrum has a continuum-like, bell-shaped form indicating that the γ decay is dominated by statistical processes in the region $E_\gamma = 1.4 - 6.5$ MeV. However, by looking at the lower panel of Fig. 4.6, it is clear that the main assumption of the subtraction method is not fulfilled for $E_\gamma \lesssim 1.4$ MeV. In this region, some strong, low-energy transitions were not subtracted correctly. This means that the levels from which these transitions originate are populated more strongly from higher excited levels through γ emission, than directly by inelastic ^{3}He scattering. Therefore, only data for $E_\gamma > 1.6$ MeV is used in the further analysis. Similar considerations are done for the V and Mo nuclei.

4.3 Extraction of level density and γ-ray strength function

For compound reactions, the following assumption has been shown to be valid: the relative probability for decay into any specific set of final states is independent of the means of formation of the compound nucleus; in other words, the compound nucleus can share its excitation energy on a relatively large number of nucleons and thus "forgets" the way of formation (see, e.g., Refs. [1, 75]). The subsequent decay of the compound states will mainly be governed by statistical rules. Therefore, the decay probability $P(E, E_\gamma)$ of a γ-ray with energy E_γ decaying from a specific excitation-energy E is proportional to the level density $\rho(E_\mathrm{f})$ at the final excitation

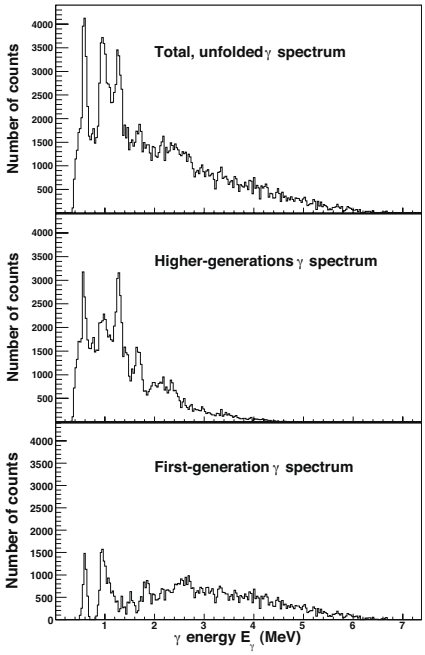

Figure 4.6: Unfolded, total γ-ray spectrum, second and higher-generation γ-ray spectrum and first-generation γ-ray spectrum of ^{45}Sc for excitation energy between $5.5 - 6.5$ MeV.

energy $E_\mathrm{f} = E - E_\gamma$, and the γ-ray transmission coefficient $\mathcal{T}(E_\gamma)$:

$$P(E, E_\gamma) \propto \rho(E_\mathrm{f})\mathcal{T}(E_\gamma). \tag{4.26}$$

The essential assumption the above relation is based on is that the nuclear reaction can be described as a two-stage process, where a compound state is first formed before it decays in a manner that is independent of the mode of formation [75, 76]. This is believed to be fulfilled at high excitation energy, even though the direct reactions (^{3}He,α) and (^{3}He,^{3}He$'$) are used, as already discussed in Sec. 4.2. Equation (4.26) can also be compared with Fermi's golden rule:

$$\lambda = \frac{2\pi}{\hbar} \left| \langle \mathrm{f} \left| \hat{H}_\mathrm{int} \right| \mathrm{i} \rangle \right|^2 \rho(E_\mathrm{f}), \tag{4.27}$$

where λ is the decay rate of the initial state $|\mathrm{i}\rangle$ to the final state $|\mathrm{f}\rangle$, and $\hat{H}_\mathrm{int}$ is the transition operator. In Eq. 4.26, an ensemble of initial and final states

within each excitation-energy bin is considered, and thus the average decay properties of a set of initial states to a set of final states.

The γ-ray transmission coefficient $\mathcal{T}(E_\gamma)$ in Eq. 4.26 is independent of the excitation energy, and thus the nuclear temperature according to the generalized Brink-Axel hypothesis [30, 36], which states that collective excitation modes built on excited states have the same properties as those built on the ground state. This hypothesis is violated when high temperatures and/or spins are involved in the nuclear reactions, as shown for GEDR excitations in Ref. [60] and references therein. However, since both the temperature reached and the spins populated are rather low for the experiments in this work, these dependencies are assumed to be of minor importance in the excitation-energy region of interest here.

To extract the level density and the γ-ray transmission coefficient, an iterative procedure [4] is applied to the first-generation γ matrix $P(E, E_\gamma)$. The basic idea of this method is to minimize

$$\chi^2 = \frac{1}{N_{\text{free}}} \sum_{E=E^{\text{min}}}^{E^{\text{max}}} \sum_{E_\gamma=E_\gamma^{\text{min}}}^{E} \left(\frac{P_{\text{th}}(E, E_\gamma) - P(E, E_\gamma)}{\Delta P(E, E_\gamma)} \right)^2, \tag{4.28}$$

where N_{free} is the number of degrees of freedom, and $\Delta P(E, E_\gamma)$ is the uncertainty in the experimental first-generation γ-ray matrix. The experimental matrix of first-generation γ-rays is normalized [4] such that for every excitation-energy bin E, the sum over all γ energies E_γ from some minimum value E_γ^{min} to the maximum value $E_\gamma^{\text{max}} = E$ at this excitation-energy bin is unity:

$$\sum_{E_\gamma=E_\gamma^{\text{min}}}^{E} P(E, E_\gamma) = 1. \tag{4.29}$$

The first-generation γ-ray matrix can theoretically be approximated by

$$P_{\text{th}}(E, E_\gamma) = \frac{\rho(E - E_\gamma)\mathcal{T}(E_\gamma)}{\sum_{E_\gamma=E_\gamma^{\text{min}}}^{E} \rho(E - E_\gamma)\mathcal{T}(E_\gamma)}. \tag{4.30}$$

The input (experimental) matrix $P(E, E_\gamma)$ and the output (theoretical) matrix $P_{\text{th}}(E, E_\gamma)$ of ^{50}V are displayed in Fig. 4.7. The limits set in the first-generation matrix for extraction are also shown. These limits are chosen to ensure that the data utilized are from the statistical excitation-energy region (E^{min}, E^{max}) and that no γ lines stemming from, e.g., yrast transitions, which might not be subtracted correctly in the first-generation method, are used in the further analysis (E_γ^{min}). Every point of the ρ and $\mathcal{T}$ functions is assumed to be an independent variable, so that the reduced χ^2 of

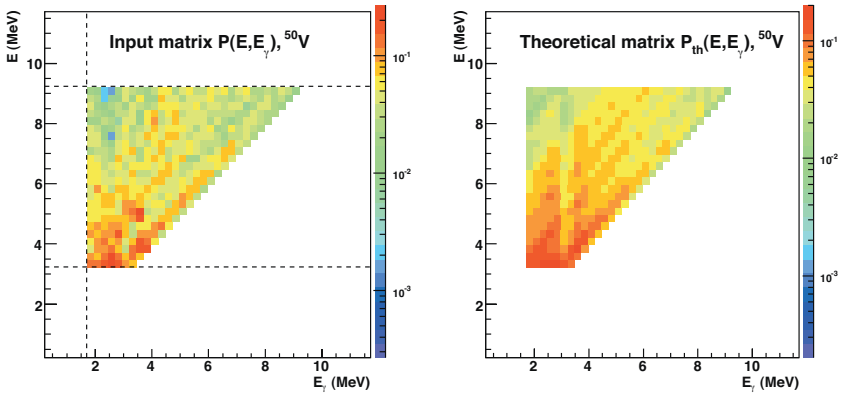

Figure 4.7: The experimental first-generation matrix $P(E, E_\gamma)$ of ^{50}V (left) and the calculated one (right) from the iteration procedure of A. Schiller *et al.* [4]. The dashed lines show the limits set in the experimental first-generation matrix.

Eq. (4.28) is minimized for every argument $E - E_\gamma$ and E. The quality of the procedure when applied to ^{50}V is shown in Fig. 4.8, where the experimental first-generation spectra for various initial excitation energies are compared to the least-χ^2 solution. In general, the agreement between the experimental data and the fit is very good.

The globalized fitting to the data points only gives the functional form of ρ and $\mathcal{T}$. In fact, it has been shown [4] that if one solution for the multiplicative functions ρ and $\mathcal{T}$ is known, one may construct an infinite number of other functions, which give identical fits to the $P(E, E_\gamma)$ matrix by

$$\tilde{\rho}(E - E_\gamma) = A \exp[\alpha(E - E_\gamma)]\, \rho(E - E_\gamma), \quad (4.31)$$

$$\tilde{\mathcal{T}}(E_\gamma) = B \exp(\alpha E_\gamma) \mathcal{T}(E_\gamma). \quad (4.32)$$

Therefore the transformation parameters α, A and B, which correspond to the physical solution, remain to be found.

4.3.1 Normalizing the level density

In order to determine the correction α to the slope of the level density and the γ-ray transmission coefficient, and to determine the absolute value A of the level density in Eq. (4.31), the ρ function is adjusted to fit the number of known discrete levels at low excitation energy and neutron (or proton)

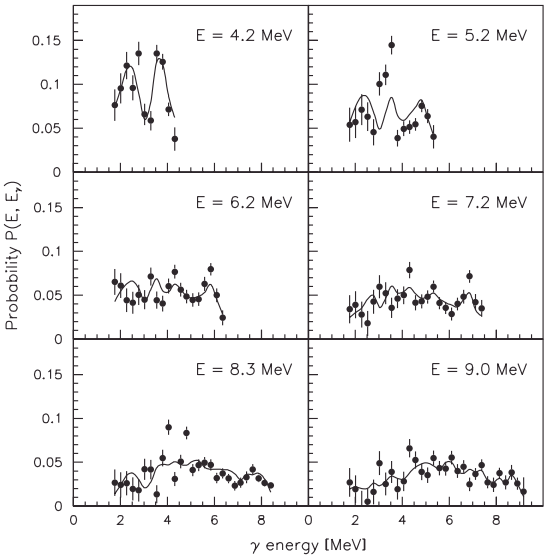

Figure 4.8: Experimental first-generation γ spectra (data points with error bars) at six different initial excitation energies (indicated in the figure) compared to the χ^2 fit (solid lines) for ^{50}V. The fit is performed simultaneously on the entire first-generation matrix of which the six displayed spectra are a fraction.

resonance data at high excitation energy. This normalization is shown for ^{44}Sc in Fig. 4.9. The data point at high excitation energy (open square in Fig. 4.9) is calculated in the following way according to [4]: The starting point are the Eqs. (4) and (5) of Ref. [16]:

$$\rho(U,J) = \frac{\sqrt{\pi}}{12}\frac{\exp(2\sqrt{aU})}{a^{1/4}U^{5/4}}\frac{(2J+1)\exp\left[-(J+1/2)^2/2\sigma^2\right]}{2\sqrt{2\pi}\sigma^3}, \tag{4.33}$$

$$\rho(U) = \frac{\sqrt{\pi}}{12}\frac{\exp(2\sqrt{aU})}{a^{1/4}U^{5/4}}\frac{1}{\sqrt{2\pi}\sigma}, \tag{4.34}$$

where $\rho(U,J)$ is the level density for a given spin J, and $\rho(U)$ is the level density for all spins (Eq. (4.34) is identical to Eq. (2.4)). The level-density parameter a and the spin cutoff parameter σ is taken from Ref. [18]. Let I be the spin of the target nucleus in a neutron resonance experiment. The average neutron resonance spacing $D_{\ell=0}$ for s-wave neutrons with

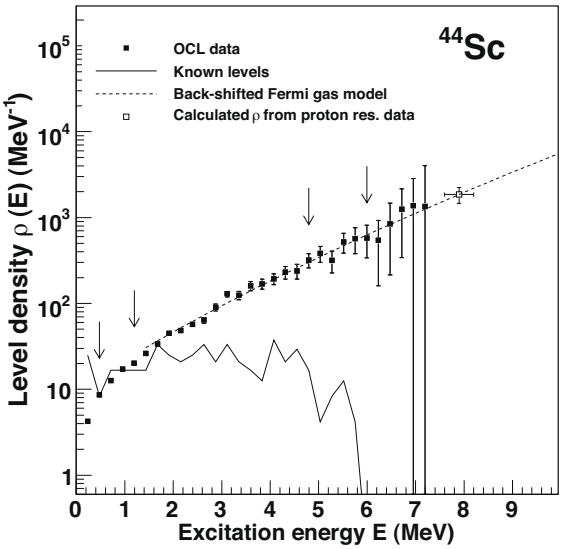

Figure 4.9: Normalization procedure of the level density (data points) of ^{44}Sc. The data points between the arrows are normalized to known levels at low excitation energy (solid line) and to the level density at the proton binding energy (open square) using an interpolation with the Fermi-gas level density (dashed line).

spin/parity $1/2^+$ can be written as

$$\frac{1}{D_0} = \frac{1}{2}\left[\rho(B_n, J = I + 1/2) + \rho(B_n, J = I - 1/2)\right], \tag{4.35}$$

because all levels with spin $J = I \pm 1/2$ are accessible in neutron resonance experiments, and it is assumed that both parities contribute equally to the level density at the neutron binding energy B_n. Combining Eqs. (4.33) to (4.35) with $U = B_n$, one finds the total level density at the neutron binding energy to be

$$\rho(B_n) = \frac{2\sigma^2}{D_0} \cdot \frac{1}{(I+1)\exp\left[-(I+1)^2/2\sigma^2\right] + \exp\left[-I^2/2\sigma^2\right]}, \tag{4.36}$$

where σ is calculated at B_n using Eq. (2.9).

Since the data only reach up to excitation energies around $B_n - E_\gamma^{\min}$, an interpolation is made between the Oslo data and $\rho(B_n)$ using the back-shifted Fermi gas model of Ref. [18], as shown in Fig. 4.9.

4.3.2 Normalizing the γ-ray transmission coefficient

The slope of the γ-ray transmission coefficient $\mathcal{T}(E_\gamma)$ has already been determined through the normalization of the level density as explained in the previous section. The remaining constant B in Eq. (4.32) gives the absolute normalization of $\mathcal{T}$, and is determined using information from neutron resonance decay on the average total radiative width $\langle\Gamma_\gamma\rangle$ at B_n according to Ref. [61].

The starting point is Eq. (3.1) of Ref. [59],

$$\langle\Gamma_\gamma(E,I,\pi)\rangle = \frac{1}{2\pi\rho(E,I,\pi)}\sum_{XL}\sum_{I_\mathrm{f},\pi_\mathrm{f}}\int_{E_\gamma=0}^{E}\mathrm{d}E_\gamma\mathcal{T}_{XL}(E_\gamma)\rho(E-E_\gamma,I_\mathrm{f},\pi_\mathrm{f}), \tag{4.37}$$

where $\langle\Gamma_\gamma(E,I,\pi)\rangle$ is the average total radiative width of levels with energy E, spin I and parity π. The summation and integration are going over all final levels with spin I_f and parity π_f that are accessible through γ transitions with energy E_γ, electromagnetic character X and multipolarity L. Assuming that the main contribution to the experimental $\mathcal{T}$ is from dipole radiation ($\ell = 1$), it can be expressed as

$$B\mathcal{T}(E_\gamma) = B\sum_{XL}\mathcal{T}_{XL}(E_\gamma) \approx B\left[\mathcal{T}_{\mathrm{E1}}(E_\gamma) + \mathcal{T}_{\mathrm{M1}}(E_\gamma)\right], \tag{4.38}$$

from which the total, experimental γ-ray strength function can easily be calculated from Eq. (2.18):

$$f(E_\gamma) = \frac{1}{2\pi E_\gamma^3}B\mathcal{T}(E_\gamma). \tag{4.39}$$

Further, we also assume that there are equally many accessible levels with positive and negative parity for any excitation energy and spin, so that the level density is given by

$$\rho(E-E_\gamma,I_\mathrm{f},\pm\pi_\mathrm{f}) = \frac{1}{2}\rho(E-E_\gamma,I_\mathrm{f}). \tag{4.40}$$

Now, by combining Eqs. (4.37), (4.38) and (4.40), the average total radiative width of neutron s-wave capture resonances with spins $I_t \pm 1/2$ expressed

in terms of $\mathcal{T}$ is obtained:

$$\langle \Gamma_\gamma(B_n, I_t \pm 1/2, \pi_t) \rangle = \frac{B}{4\pi\rho(B_n, I_t \pm 1/2, \pi_t)} \int_{E_\gamma=0}^{B_n} \mathrm{d}E_\gamma \mathcal{T}_{XL}(E_\gamma) \times \rho(B_n - E_\gamma) \sum_{J=-1}^{1} g(B_n - E_\gamma, I_t \pm 1/2 + J), \tag{4.41}$$

where I_t and π_t are the spin and parity of the target nucleus in the (n, γ) reaction and $\rho(B_n - E_\gamma)$ is the experimental level density. Note that the factor $1/\rho(B_n, I_t \pm 1/2, \pi_t)$ equals the neutron resonance spacing D_0. The spin distribution of the level density is given by [16]:

$$g(E, I) = \frac{2I+1}{2\sigma^2} \exp\left[-(I+1/2)^2/2\sigma^2\right]. \tag{4.42}$$

The spin distribution is normalized so that $\sum_I g(E, I) \approx 1$. The experimental value of $\langle \Gamma_\gamma \rangle$ at B_n is then the weighted sum of the level widths of states with $I_t \pm 1/2$ according to Eq. (4.41). From this expression the normalization constant B can be determined as described in Ref. [61]. However, some considerations must be done before normalizing according to Eq. (4.41).

Methodical difficulties in the primary γ-ray extraction prevent determination of the function $\mathcal{T}(E_\gamma)$ for $E_\gamma < E_\gamma^{\min}$ as discussed previously. In addition, the data at the highest γ-energies in the interval $B_n - E_\gamma^{\min} \leq E_\gamma \leq B_n$ suffer from poor statistics. Therefore, $\mathcal{T}$ is extrapolated with an exponential function, as demonstrated for ^{51}V in Fig. 4.10. The contribution of the extrapolation to the total radiative width given by Eq. (4.41) does not normally exceed 15%, thus the errors due to a possibly poor extrapolation are expected to be of minor importance [61].

4.4 Possible uncertainties in the normalization procedures

4.4.1 The spin distribution

The quantity $\rho(B_n)$ is calculated assuming a bell-like spin distribution according to [16] given by Eq. (4.42) and using a model for the spin cutoff parameter σ taken from [16] in the case of the Mo and V nuclei, and from [18] for the Sc isotopes. Both these assumptions could in principle be a

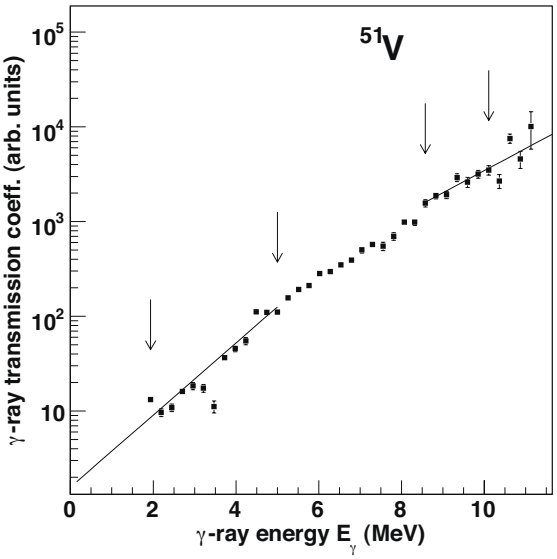

Figure 4.10: Extrapolation of the γ-ray transmission coefficient of ^{51}V. The data points between the arrows in the low and high γ-energy regions are utilized to fit the exponential functions to the data.

source of uncertainty, as it is hard or even impossible to measure the total spin distribution experimentally at high excitation energy.

In Fig. 4.11 various spin distributions for ^{44}Sc are shown, calculated at an excitation energy of 8.0 MeV. In the two upper panels, the spin distribution of [16] has been used, but with the expression for the spin cutoff parameter of [16] given in Eq. (2.5) in panel a) and the formalism of [18] (Eq. (2.9)) in panel b). In panel c) the spin distribution the spin-dependent level densities of [23] are shown. Here, the authors also have assumed a bell-shaped spin distribution according to Eqs. (7) and (8) in [23]. It is clear from the figure that the spin distributions in panel b) and c) give a broader spin distribution and a centroid shifted to higher spins compared to the one in panel a).

In panel d), the spin distribution of the calculated spin- and parity-dependent level density of [25] briefly discussed in Sec. 2.1 is shown. There are no underlying assumptions for the spin distribution in these calculations. It is seen from this distribution that there is a significant difference

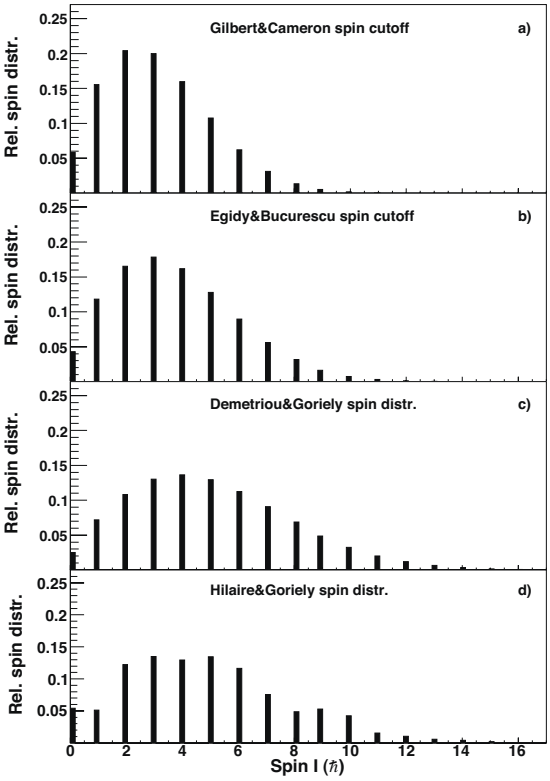

Figure 4.11: Relative spin distributions calculated for $E = 8.0$ MeV of ^{44}Sc (see text).

in the relative numbers of states with spin 0 and 1. The normalization method for the level density described above is especially sensitive to such variations at low spin if the neutron resonance spacing D_0 is measured from a neutron capture reaction where the target nucleus is even-even, that is, with zero ground-state spin. Then the states reached in neutron capture can only have spin $1/2^+$, and the number of all other states must be estimated using a certain spin cutoff parameter, introducing a larger uncertainty in the calculated $\rho(B_n)$. Therefore it is preferred to calculate $\rho(B_n)$ from both D_0 and D_1 resonance spacings if possible, since in the latter, also states with $3/2^-$ are reached for target nuclei with $I^\pi = 0^+$, and will therefore decrease this uncertainty.

4.4.2 The parity distribution

As described above, for both the normalization of the level density and the γ-ray transmission coefficient the assumption of equally many levels with positive and negative parity is used. For the level density, this assumption is likely to be approximately valid since it is utilized for the calculation of $\rho(B_n)$, which is at relatively high excitation energies for the nuclei considered in this work (see Table 3.4). For the nuclei ^{44,45}Sc and $^{93-98}$Mo, this assumption has been investigated by calculating the parity distribution with the code 'Micro' presented in [10]. Using ρ_+ and ρ_- to denote the level density with positive and negative parity levels, the parity asymmetry α is defined as [71]

$$\alpha = \frac{\rho_+ - \rho_-}{\rho_+ + \rho_-}, \tag{4.43}$$

which gives -1 and 1 for only negative and positive parities, respectively, and 0 when both parities are equally represented.

The resulting parity distributions are shown in Figs. 4.12 and 4.13 for the Sc and Mo isotopes. It is seen in Fig. 4.12 that α is close to zero for $E \approx 10$ MeV for both ^{44,45}Sc, in excellent agreement with the findings of [71]. By inspecting the $2^+/2^-$ level densities in ^{58}Ni and ^{90}Zr (Ref. [72] and references therein), one sees that this is also the case for these nuclei. However, the calculations for the Mo isotopes indicate a majority of levels with positive parity, even at excitation energies around 8 MeV, in conflict with the ^{90}Zr data and the calculations of [25].

To investigate the impact of the assumption of parity symmetry on the calculations of $\rho(B_n)$, the ratio ρ_+/ρ_- as a function of the parity asymmetry α is defined from Eq. (4.43) as

$$\frac{\rho_+}{\rho_-} = \frac{1+\alpha}{1-\alpha}. \tag{4.44}$$

Inserting $\alpha \approx 0.3$ found in the calculations on ^{93}Mo, we get

$$\rho_+ \approx 2 \cdot \rho_-, \tag{4.45}$$

which means that the assumption of equally many positive and negative parity levels are clearly not fulfilled in the 'Micro' calculations.

The parity distribution should be taken into account when calculating $\rho(B_n)$ for cases where the parity asymmetry is large. If one assumes that the spin- and parity-projected level density $\rho(E, J, \pi)$ can be described by [73]

$$\rho(E, J, \pi) = \rho(E) \cdot g(E, J) \cdot \mathcal{P}(E, \pi), \tag{4.46}$$

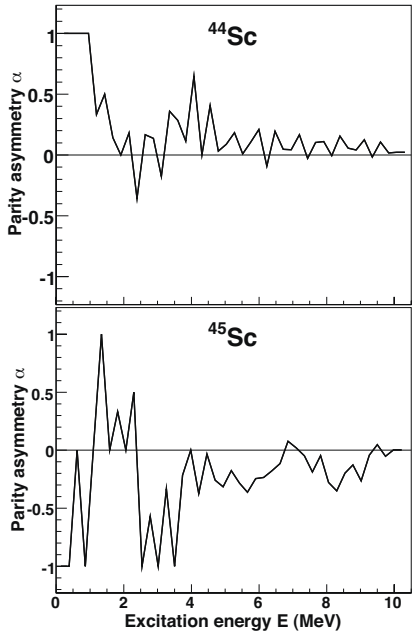

Figure 4.12: Parity distributions as a function of excitation energy calculated for ^{44,45}Sc (see text).

where $\rho(E)$ is the total level density at excitation energy E, $g(E,J)$ is the spin distribution given by Eq. (4.42), and $\mathcal{P}(E,\pi)$ is the parity projection factor. According to Eq. (4.35), we get

$$\frac{1}{D_0} = \rho(B_n) \cdot g(B_n, J = I \pm 1/2) \cdot \mathcal{P}(B_n, \pi_t) \tag{4.47}$$

for the neutron resonance spacing at B_n reaching states with parity $\pi_t \cdot (-1)^\ell = \pi_t$ for s-wave neutrons having $\ell = 0$. Now, defining the level density of levels with the same parity π_g as the ground state of the nucleus as ρ_g, and the level density of levels with parity π_s opposite to the ground state of the nucleus as ρ_s, we obtain [73]

$$\mathcal{P}_g \equiv \mathcal{P}(E, \pi = \pi_g) = \frac{\rho_g}{\rho} = \frac{1}{1+\xi}, \tag{4.48}$$

$$\mathcal{P}_s \equiv \mathcal{P}(E, \pi = \pi_s) = \frac{\rho_s}{\rho} = \frac{1}{1+1/\xi}, \tag{4.49}$$

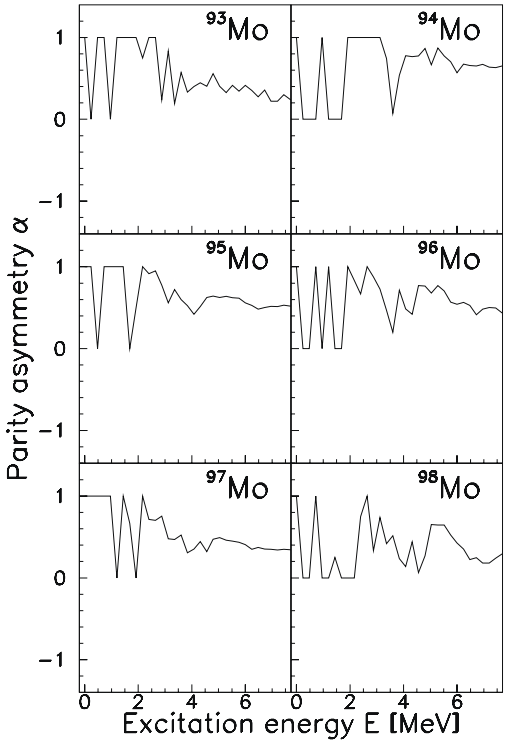

Figure 4.13: Parity distributions as a function of excitation energy calculated for $^{93-98}$Mo (see text).

with

$$\xi = \frac{\rho_s}{\rho_g}. \tag{4.50}$$

Further,

$$\frac{1}{D_0} = \rho(B_n)\left[g(B_n, J = I + 1/2) + g(B_n, J = I - 1/2)\right]\mathcal{P}_g(B_n) \tag{4.51}$$

$$= \rho(B_n)\left[g(B_n, J = I + 1/2) + g(B_n, J = I - 1/2)\right]\frac{1}{1+\xi}, \tag{4.52}$$

which gives

$$\rho(B_n) = \frac{\sigma^2}{D_0} \frac{1+\xi}{(I+1)\exp\left[-(I+1)^2/2\sigma^2\right] + I\exp\left[-I^2/2\sigma^2\right]}, \tag{4.53}$$

using Eq. (4.42). In the future, the expression given in Eq. (4.53) should be used for the calculation of $\rho(B_n)$ instead of Eq. (4.35) if the parity asymmetry is known, and especially if the parity asymmetry at B_n is large. The estimation of the factor ξ should be based on experimental data, or on realistic calculations if such data are not available.

The assumption of equally distributed levels with positive and negative parity influence also the normalization of the γ-ray transmission coefficient. To take into account the parity distribution, one can modify Eq. (4.40) according to Eq. (4.46) so that

$$\rho(E - E_\gamma, I_\mathrm{f}, \pm\pi_\mathrm{f}) = \rho(E - E_\gamma) \cdot g(E - E_\gamma, I_\mathrm{f}) \cdot \mathcal{P}_g(E - E_\gamma, \pi_\mathrm{f}). \tag{4.54}$$

Instead of Eq. (4.41), one finds

$$\begin{aligned}\langle \Gamma_\gamma(B_n, I_t \pm 1/2, \pi_t)\rangle =& \frac{B}{2\pi\rho(B_n, I_t \pm 1/2, \pi_t)} \int_{E_\gamma=0}^{B_n} \mathrm{d}E_\gamma \mathcal{T}_{XL}(E_\gamma) \\ &\times \rho(B_n - E_\gamma) \sum_{J=-1}^{1} g(B_n - E_\gamma, I_t \pm 1/2 + J)\mathcal{P}_g(B_n - E_\gamma, \pi_\mathrm{f}),\end{aligned} \tag{4.55}$$

where $\mathcal{P}_g$ now must be evaluated for every argument $B_n - E_\gamma$.

4.5 Robustness test of the Oslo method

The nucleus ^{96}Mo has become a benchmark for other experimental groups trying to verify or falsify the upbend structure seen in the γ-ray strength function [9]. For ^{96}Mo, it has been discovered that the extraction of the first-generation spectra used in Ref. [9] was not performed in an optimal way, and therefore the data sets from the reactions ^{96}Mo(^{3}He,^{3}He$'\gamma$)^{96}Mo and ^{97}Mo(^{3}He,$\alpha\gamma$)^{96}Mo have recently been reanalyzed [74]. The two main reasons for reanalyzing these data are explained in the following.

In the previous analysis, the γ-ray energies close or below the strong 778.2 keV $2^+ \rightarrow 0^+$ ground-state band transition were included, and this transitional region in the experimental (E, E_γ) matrix were not properly subtracted in the first-generation procedure. These γ-ray energies are now excluded from the further analysis.

The second point concerns the estimate of the γ-ray multiplicity as function of excitation energy, which was used for the normalization procedure in the first-generation method as explained in Sec. 4.2. In the previous analyses, the statistical multiplicity at excitation energy E was estimated by introducing a lower γ-ray threshold E_0 and an effective excitation energy $E - E_{\text{entry}}$ giving

$$\langle M_\gamma^{\text{stat}} \rangle = (E - E_{\text{entry}}) / \langle E_\gamma \rangle_{>E_0}, \tag{4.56}$$

where $\langle E_\gamma \rangle_{>E_0}$ is the average energy of the γ spectrum for $E_\gamma > E_0$. The E_{entry} parameter mimics the excitation energy at which the statistical γ-ray transitions enter the ground-state band. This treatment is applicable to rare earth nuclei, where the CACTUS efficiency for the lowest ground state band transitions, typically the $4^+ \rightarrow 2^+$ and the $2^+ \rightarrow 0^+$ transitions, is low. However, for ^{96}Mo the energy of the lowest ground-state band transitions are detected with high efficiency, as the first excited state is at $E = 778.2$ keV [26]. Therefore, in the present analysis the straightforward expression for the total γ-ray multiplicity

$$\langle M_\gamma^{\text{tot}} \rangle = E / \langle E_\gamma \rangle, \tag{4.57}$$

is used, where the excitation energy is simply divided by the average energy of the γ spectrum as in Eq. (4.21).

In Figs. 4.14 and 4.15 the reanalyzed level densities and γ-ray strength functions are compared with previous data [9, 13]. Note that the error bars include statistical errors only. A very good resemblance between the pick-up reaction and the inelastic scattering reaction is seen. The reanalyzed level densities are very similar to the previous ones, and the same is true for the γ-ray strength functions, except that the upbend is less pronounced due to the exclusion of the 778.2 keV transition. This gives further confidence in the robustness and stability of the Oslo method, as different ways of performing the analysis give very similar results.

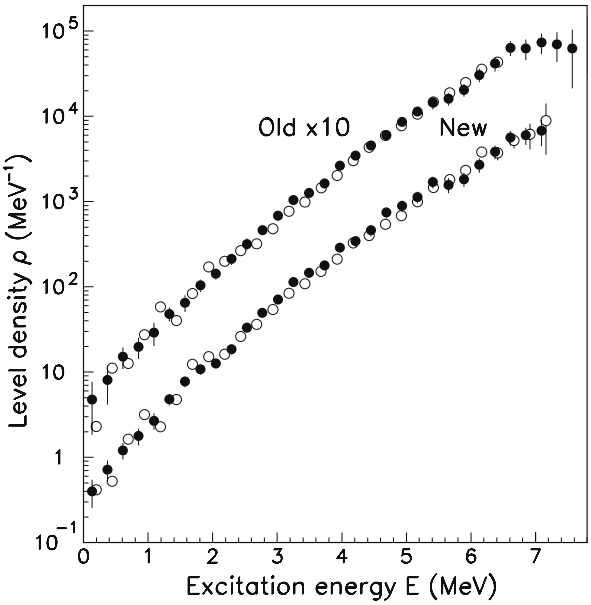

Figure 4.14: Experimental level densities of ^{96}Mo from the (^{3}He,α) (filled circles) and the (^{3}He,^{3}He′) (open circles) reaction. The data from the new analysis is compared with previously published data [13].

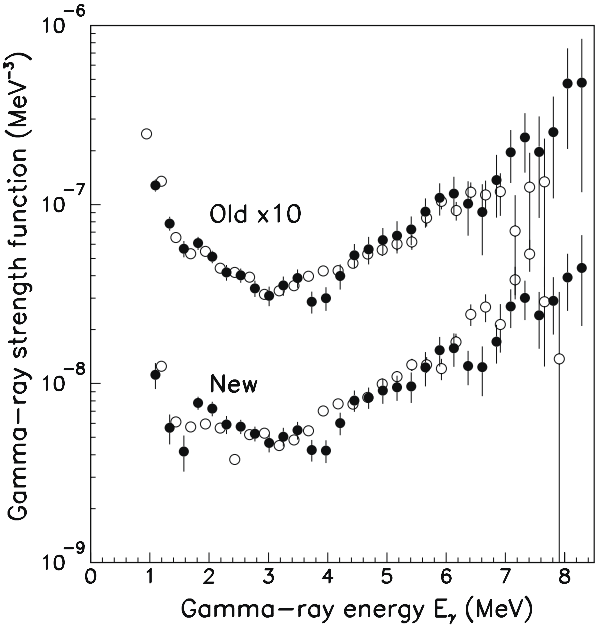

Figure 4.15: Experimental γ-ray strength functions of ^{96}Mo from the (^{3}He,α) (filled circles) and the (^{3}He,^{3}He′) (open circles) reaction. The data from the new analysis is compared with previously published data [9].

Chapter 5

Papers

The following papers are included in this thesis:

1. M. Guttormsen, R. Chankova, U. Agvaanluvsan, E. Algin, L.A. Bernstein, F. Ingebretsen, T. Lönnroth, S. Messelt, G.E. Mitchell, J. Rekstad, A. Schiller, S. Siem, A.C. Sunde[1], A. Voinov and S. Ødegård, *Radiative strength functions in* $^{93-98}$Mo, Phys. Rev. C **71**, 044307 (2005).

2. R. Chankova, A. Schiller, U. Agvaanluvsan, E. Algin, L. A. Bernstein, M. Guttormsen, F. Ingebretsen, T. Lönnroth, S. Messelt, G. E. Mitchell, J. Rekstad, S. Siem, A. C. Larsen, A. Voinov, and S. W. Ødegård, *Level densities and thermodynamical quantities of heated* $^{93-98}$Mo *isotopes*, Phys. Rev. C **73**, 034311 (2006).

3. A. C. Larsen, R. Chankova, M. Guttormsen, F. Ingebretsen, T. Lönnroth, S. Messelt, J. Rekstad, A. Schiller, S. Siem, N. U. H. Syed, A. Voinov, and S. W. Ødegård, *Microcanonical entropies and radiative strength functions of* ^{50,51}V, Phys. Rev. C **73**, 064301 (2006).

4. A. C. Larsen, M. Guttormsen, R. Chankova, F. Ingebretsen, T. Lönnroth, S. Messelt, J. Rekstad, A. Schiller, S. Siem, N. U. H. Syed, and A. Voinov, *Nuclear level densities and γ-ray strength functions in* ^{44,45}Sc, Phys. Rev. C **76**, 044303 (2007).

5. A. V. Voinov, S. M. Grimes, A. C. Larsen, C. R. Brune, M. Guttormsen, T. Massey, A. Schiller, S. Siem, and N. U. H. Syed, *Level densities of* ^{44}Sc *and* ^{47}Ti *from different experimental techniques*, Phys. Rev. C **77**, 034613 (2008).

[1] I changed my last name from 'Sunde' to 'Larsen' in 2006.

5.1 Brief introduction to the papers

Paper 1 and 2: The Mo isotopes

The motivation for the Mo experiments was primarily to test the Oslo method in the mass region near the $N = 50$ shell closure. Also, as the ground-state deformation parameter β_2 goes down from 0.17 in ^{98}Mo to 0.11 in ^{92}Mo [19], one would expect to see deformation effects in both the level density (decreasing $\rho(E)$ as the deformation decreases) and the γ-ray strength function (decreasing $f(E_\gamma)$ as the deformation decreases since the tail of the GEDR is expected to decrease when approaching spherical nuclear shape).

In paper 1, the γ-ray strength functions of $^{93-98}$Mo were studied through the analysis of the measured (^{3}He,^{3}He$'\gamma$) and (^{3}He,$\alpha\gamma$) reactions as described in Chapters 3 and 4. It was found that the γ-ray strength functions agreed well with the low-energy tail of the GEDR for γ-ray energies larger than about 3 MeV. However, below $E_\gamma \approx 3$ MeV, an increase of the strength functions was found for all nuclei, similar to the behavior previously discovered in ^{56,57}Fe [8]. This feature was found to be present at all initial excitation energies between $5 - 8$ MeV.

In paper 2, the level densities of $^{93-98}$Mo were investigated and analyzed within the framework of thermodynamics. It was found that the level density decreased when approaching the $N = 50$ shell closure. For example, $\rho(6\,\text{MeV}) \approx 4000\,\text{MeV}^{-1}$ for ^{98}Mo, while $\rho(6\,\text{MeV}) \approx 1400\,\text{MeV}^{-1}$ for ^{94}Mo. Also, the level densities of ^{93,94}Mo display more structures than the heavier Mo isotopes.

Thermodynamic quantities such as entropy, temperature, and heat capacity were deduced using both the microcanonical and canonical ensemble, and signatures of phase transitions were looked for (see Appendix B). The difference in the microcanonical entropies of $^{93-94}$Mo were found to be close to zero, while for $^{97-98}$Mo it was about $1k_B$. These observations were qualitatively explained considering the available single-particle orbits in the two cases. The canonical heat capacities showed an *S*-like functional form that might indicate a pairing phase transition, consistent with shell-model Monte Carlo simulations.

Paper 3: The V isotopes

In light of the successful application of the Oslo method on Fe and Mo nuclei, ^{51}V with $N = 28$ was chosen for the next experimental campaign at OCL. Now, the enhancement in the γ-ray strength function at low γ-

ray energies had been discovered not only in ^{56,57}Fe, but also in all the Mo isotopes studied in paper 1. One could therefore suspect that this feature was not singular for Fe and Mo due to some specific nuclear-structure effects in these nuclei, but rather could be a general feature, perhaps some sort of low-energy resonance, in a certain mass region.

The level densities and γ-ray strength functions of ^{50,51}V measured using the Oslo method on the (^{3}He,^{3}He$'\gamma$) and (^{3}He,$\alpha\gamma$) coincidence spectra. The level density of ^{51}V showed distinct structures and bumps at excitation energies up to $\approx$ 4.5 MeV, interpreted as effects of the $N = 28$ shell closure that inhibit the neutrons from participating in the creation of levels until the excitation energy is high enough to let the neutrons cross the shell gap. Microcanonical entropies were deduced from the level densities, and the entropy difference were found to be about $1.2k_B$. The γ-ray strength functions resembled the ones in Fe and Mo, with a good agreement with the low-energy GEDR tail at high γ-ray energies and an enhancement at low γ-ray energies.

Paper 4 and 5: The Sc isotopes

Going even further down in mass number and approaching the $Z = 20$ major shell, the level densities and γ-ray strength functions of the nuclei ^{44,45}Sc were extracted from the (^{3}He,^{3}He$'\gamma$) and (^{3}He,$\alpha\gamma$) data taken at OCL. The results were presented in paper 4. The level densities of both nuclei turned out to be much less structured than for ^{51}V, in spite of them having only one proton above the $Z = 20$ shell. However, the neutrons are mid-shell in the $1f_{7/2}$ orbit, and, apparently, produce a rather smooth behavior of the level density function. The level densities were compared with calculations performed with a microscopic combinatorial model called 'Micro', where BCS quasi-particles are scattered randomly into Nilsson single-particle levels, and collective states were schematically added. The agreement with this very simple model was satisfactory, especially for ^{44}Sc. Also the average number of broken Cooper pairs and the parity asymmetry were extracted from the calculations. The γ-ray strength functions were compared to (γ,n) and (γ,p) data and to the theoretical GEDR tail, and a good agreement was again found at γ-ray energies above 4 MeV. The γ-ray strength functions are seen to increase for γ-ray energies below 4 MeV, and this upbend structure is shown to be independent of initial excitation energy for $E = 4.5 - 9.3$ MeV in ^{45}Sc. Thus, the existence of this structure has been established in twelve nuclei from four different elements (Sc, V, Fe and Mo).

The motivation for the particle-evaporation experiment at Ohio University presented in paper 5 was twofold. First, since the normalization of the level density in ^{44}Sc was based on proton resonances with no distinction of $\ell = 0, 1$, this normalization might prove wrong even though a reasonable agreement was found with the level density and strength function of ^{45}Sc. By performing a particle-evaporation experiment for the compound reaction ^{45}Sc(^{3}He,α)^{44}Sc, where the α particles were measured in *backward* angles, the level density could be extracted using a Hauser-Feshbach model to describe the measured evaporation spectra. This method, which is briefly described in Chapter 2, will give the slope of the level density directly without any input from auxiliary data except the particle transmission coefficients determined from optical potential models. Thus, an independent check of the slope of the ^{44}Sc level density and strength function could be obtained.

Second, the overall agreement between the level density of ^{56}Fe previously measured at OCL and Ohio University was very good [28]. Therefore, we wanted to see if this was also the case for ^{44}Sc. The results presented in paper 5 was very encouraging, as the slope of the level density utilized in the OCL data was verified, and the agreement between the OCL and Ohio data were excellent (see also Fig. 2.2). The reliability of the Oslo method is thus further strengthened.